RL-TR-97-5, Vol II (of two)
Final Technical Report
May 1997


# MULTICHANNEL SYSTEM IDENTIFICATION AND DETECTION USING OUTPUT DATA TECHNIQUES

Scientific Studies Corporation

Jaime R. Roman and Dennis W. Davis



*APPROVED FOR PUBLIC RELEASE; DISTRIBUTION UNLIMITED.*



Rome Laboratory
Air Force Materiel Command
Rome, New York

Although this report references limited document RL-TR-91-162, no limited information has been extracted.

This report has been reviewed by the Rome Laboratory Public Affairs Office (PA) and is releasable to the National Technical Information Service (NTIS). At NTIS it will be releasable to the general public, including foreign nations.

RL-TR-97-5, Vol II has been reviewed and is approved for publication.

APPROVED: James H. Michels

JAMES H. MICHELS
Project Engineer

FOR THE COMMANDER: Donald W. Hanson

DONALD W. HANSON, Director
Surveillance & Photonics Directorate

If your address has changed or if you wish to be removed from the Rome Laboratory mailing list, or if the addressee is no longer employed by your organization, please notify RL/OCSM, 26 Electronic Pky, Rome, NY 13441-4514. This will assist us in maintaining a current mailing list.

Do not return copies of this report unless contractual obligations or notices on a specific document require that it be returned.

| REPORT DOCUMENTATION PAGE | Form Approved OMB No. 0704-0188 |
|---|---|



| 1. AGENCY USE ONLY *(Leave blank)* | 2. REPORT DATE | 3. REPORT TYPE AND DATES COVERED |
|---|---|---|
| | May 97 | FINAL Jul 93 - Oct 96 |

**4. TITLE AND SUBTITLE**

MULTICHANNEL SYSTEM IDENTIFICATION AND DETECTION USING OUTPUT DATA TECHNIQUES, VOLUME II

**5. FUNDING NUMBERS**

C - F30602-93-C-0193
PE- 65502F
PR- 3005
TA- RC
WU- 92

**6. AUTHOR(S)**

Jaime R. Roman
Dennis W. Davis

**7. PERFORMING ORGANIZATION NAME(S) AND ADDRESS(ES)**

Scientific Studies Corp.
2250 Quail Ridge
Palm Beach Gardens, FL 33418

**8. PERFORMING ORGANIZATION REPORT NUMBER**

N/A

**9. SPONSORING/MONITORING AGENCY NAME(S) AND ADDRESS(ES)**

Rome Laboratory/OCSM
26 Electronic Parkway
Rome NY 13441-4514

**10. SPONSORING/MONITORING AGENCY REPORT NUMBER**

RL-TR-97-5, Vol II

**11. SUPPLEMENTARY NOTES**

Rome Laboratory Project Engineer: James H. Michels, OCSM, 315-330-4432

**12a. DISTRIBUTION AVAILABILITY STATEMENT**

Approved for public release; Distribution unlimited.

**12b. DISTRIBUTION CODE**

**13. ABSTRACT** *(Maximum 200 words)*

The multichannel innovations-based detection algorithm (MIBDA) methodology formulated in Phase I was developed in full and evaluated in the context of two applications: (a) airborne surveillance phased array radar systems, and (b) computer-based electrocardiogram (ECG) diagnosis. A software simulation was developed to generate simulated multichannel phased array radar data. This software was exercised to represent ground clutter as the output of a state variable model (SVM), and to assess the performance of such models in the MIBDA. The MIBDA was modified and extend to the automated diagnosis of ECG traces. MIBDA performance for ECG diagnosis was assessed using the Common Standards for Quantitative Electrocardiography (CSE) database. Analysis and simulation results indicate that the MIBDA offers a valid alternative to conventional systems in both of the applications considered. This suggests also that the MIBDA can be configured to apply to a wide range of problem areas. Volume I presents the MIBDA methodology, SVM identification algorithms, MIBDA design and performance evaluation issues, and simulation results for both applications. Volume II presents the analytic and software model for airborne surveillance phased array radar systems.

| 14. SUBJECT TERMS | 15. NUMBER OF PAGES |
|---|---|
| Multichannel Detection, Airborne Surveillance, State-Space Model, Innovations Processes, System Identification, ECG Diagnostics | 76 |
| | 16. PRICE CODE |

| 17. SECURITY CLASSIFICATION OF REPORT | 18. SECURITY CLASSIFICATION OF THIS PAGE | 19. SECURITY CLASSIFICATION OF ABSTRACT | 20. LIMITATION OF ABSTRACT |
|---|---|---|---|
| UNCLASSIFIED | UNCLASSIFIED | UNCLASSIFIED | SAR |

## TABLE OF CONTENTS

## LIST OF FIGURES

## LIST OF TABLES

## 1.0 INTRODUCTION

This document is Volume II of a two-volume Final Technical Report which summarizes a major task carried out by the Scientific Studies Corporation (SSC) in Phase II of the "Multichannel System Identification and Detection Using Output Data Techniques" Small Business Innovation Research (SBIR) program for Rome Laboratory (RL). The companion Volume I presents the formulations, analyses, and simulation results obtained in the program (Román and Davis, 1996). Distribution of Volume I is limited as dictated by the standard SBIR regulations, whereas distribution of this volume is unlimited.

This volume discusses the analytic and software (MATLAB-based) model for the multichannel output waveform in airborne surveillance phased array radar systems. Specifically, target, jamming (spatially-localized, broadband interference), receiver noise, and ground clutter components are modeled. Of these components, ground clutter is the most difficult to model in the context of surveillance array radar. The ground clutter model follows the approach used by Jaffer et al. (1991), and more recently by Ward (1994).

A description of the SSC model-based multichannel detection methodology in the context of space/time processing for phased array radar systems is provided in Volume I (Román and Davis, 1996). In order to validate the methodology and to evaluate alternative model identification algorithms in the context of space/time radar applications it is necessary to have either real or simulated radar data. Since real data was unavailable to this program, SSC developed analytic and software models to generate simulated data. For the purposes of this program it suffices that the simulated data be "representative" of real data, while placing modest requirements on computer resources (storage; execution

time). The software model should be flexible, in order to admit future enhancements in a straightforward manner. Additionally, the model must include a representation for the "true" channel output covariance matrix sequence to allow determination of performance in the "known covariance" case. This latter feature is important for algorithm evaluation, and is unavailable with real data.

The conditions and assumptions for the model formulation are described in Section 2.0, and the true covariance model and the data generation model are presented for each component (signal; jamming; noise; clutter). Simulation results are presented in Section 3.0 to allow comparison with corresponding results presented by Ward (1994). A summary and suggestions for further work are presented in Section 4.0.

## 2.0 AIRBORNE SURVEILLANCE PHASED ARRAY RADAR MODEL

Airborne surveillance for moving target detection using phased array radar is one of the major thrusts at RL. Consequently, the scenarios and systems considered in the model defined herein reflect that significance. The model is defined for a side-looking phased array radar configuration, with scanning capability of ±90 deg from boresight. Each component (target; noise; jammer; clutter) is modeled independently of the others. The structure selected to model each component allows generation of the true covariance matrix sequence, as well as generation of independent statistical data realizations.

Moving targets are modeled as point targets in azimuth and elevation, and each moving target is modeled as the output of a first-order linear system in state-space form. This allows for a wide range of conditions (including Swerling Cases 1 through 4 as well as the deterministic case), in a simple and general format. With this structure $G_s$ targets are grouped as a $G_s$th-order linear system. Barrage-type jammers are considered, and modeled as point sources of Gaussian-distributed broadband noise in azimuth and elevation. Receiver noise is modeled as uncorrelated in time (pulse-to-pulse) as well as in space (channel-to-channel). Ground clutter is modeled based on the principle of a large number of statistically-independent clutter patches, and each clutter patch consists of a large number of individual re-radiators.

### 2.1 Scenario Description and Problem Formulation

Consider a linear array radar consisting of $J$ equally-spaced, identical antenna elements (or identical beamformed sub-arrays) in a side-looking configuration on a surveillance platform moving at a constant velocity $V_p$ in level flight at an altitude $H_p$. Such a scenario is depicted in Figure 2-1. As suggested in Figure 2-1,

the array is aligned with the aircraft's longitudinal axis, and the aircraft velocity makes a positive crab angle $\gamma$ with the aircraft's longitudinal axis. For transmission, a power pattern $G_t(\phi,\theta)$ is assumed for the array, where $\phi$ is the azimuth angle, and $\theta$ is the elevation angle. The array main beam can be steered in azimuth and elevation, with a positive main beam azimuth angle $\phi_0$ measured clockwise from the array boresight (a positive-valued $\phi_0$ is shown in Figure 2-1), and a positive main beam elevation angle $\theta_0$ defined as a rotation up from the local horizontal plane at the radar array location (a negative-valued $\theta_0$ is shown in Figure 2-1). For simplicity, the elevation dimension is ignored herein, and the clutter return is calculated for the mainbeam elevation only. Thus, the antenna power pattern used to generate the ground clutter model is $G_t(\phi,\theta_0)$. The radar array is radiating a coherent pulse train at a constant radiation frequency $f_C$ (with corresponding radiation wavelength $\lambda_C$), and a constant pulse repetition frequency (PRF) $f_{PRF}$. For reception, the power pattern of each individual linear array element (or sub-array beamformed into a linear array) is denoted as $g_r(\phi,\theta)$; as in transmission, the receive power pattern is restricted to the mainbeam elevation only, $\theta = \theta_0$.

It is assumed that the range to moving targets, ground, and to broadband interference sources is large, so that each wavefront arriving at the array is flat (in the scale of $\lambda_C$). This is true for most surveillance scenarios. It is assumed also that each of the received wavefronts is statistically stationary (in the wide sense) for N pulses from a given range gate, the duration of one coherent processing interval (CPI). The 4/3 Earth approximation (Nathanson, 1991) is adopted for determination of the grazing angle, $\psi_c$. Table 2-1 lists all variables (physical; scenario; system) utilized in the model; this table also includes the key parameters associated with the return from a clutter patch (normalized spatial and Doppler frequencies; geometry parameters).

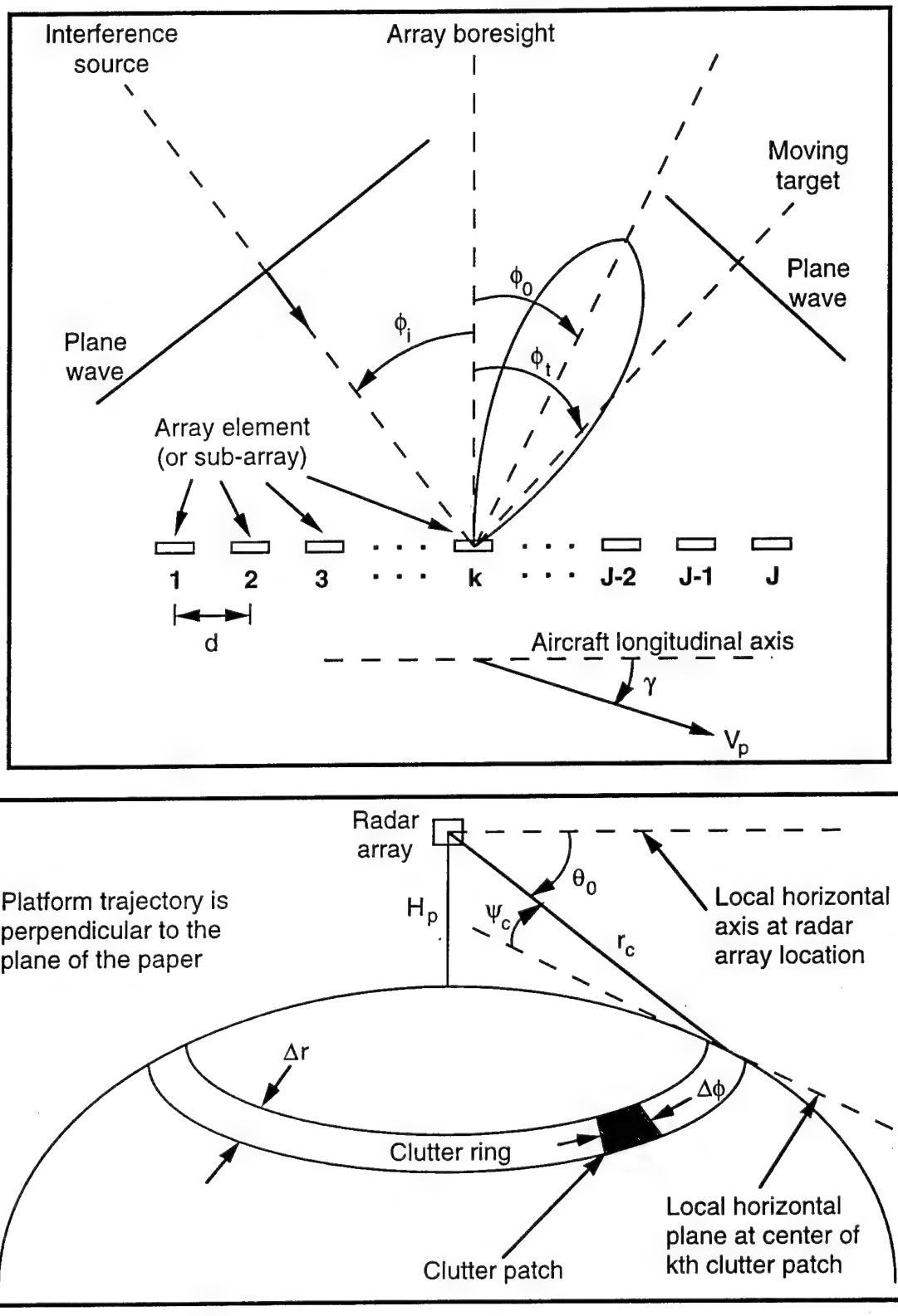


*Figure 2-1. Airborne surveillance scenario and geometry.*

Spatial frequency:

$$f_s = \frac{d}{\lambda_C}\cos(\theta)\sin(\phi) = 0.5\cos(\theta)\sin(\phi) \qquad d = \frac{\lambda_C}{2}$$

Normalized Doppler frequency:

$$f_D = \frac{2V_p}{\lambda_C}\cos(\theta)\sin(\phi - \gamma) \qquad \upsilon = \frac{4V_p}{f_{PRF}\lambda_C}$$

$$f_d = \frac{f_D}{f_{PRF}} = \frac{2V_p}{f_{PRF}\lambda_C}\cos(\theta)\sin(\phi - \gamma) = 0.5\,\upsilon\cos(\theta)\sin(\phi - \gamma)$$

Clutter patch parameters

$$\Delta r = \frac{\rho_r}{\cos(\psi_c)} \qquad \Delta\phi = \frac{2\pi}{N_c}$$

$$\theta_0 = -\sin^{-1}\left[\frac{r_c^2 + H_p(H_p + 2r_E)}{2r_c(H_p + r_E)}\right]$$

$$\psi_c = \sin^{-1}\left[\frac{H_p}{r_c}\left(1 + \frac{H_p}{2r_E}\right) - \frac{r_c}{2r_E}\right]$$

$\phi_0$ : mainbeam clutter return azimuth angle (shown positive in Figure 2-1)
$\phi_t$ : target return azimuth angle (shown positive in Figure 2-1)
$\phi_i$ : interference source azimuth angle (shown negative in Figure 2-1)
$\theta_0$ : mainbeam clutter return elevation angle (shown negative in Figure 2-1)
$\theta_t$ : target return elevation angle (not shown in Figure 2-1)
$\theta_i$ : interference source elevation angle (not shown in Figure 2-1)
$\gamma$ : aircraft platform crab angle (shown positive in Figure 2-1)
$V_p$ : platform velocity
$H_p$ : platform altitude
$V_t$ : target radial velocity (not shown in Figure 2-1)
$d$ : array inter-element spacing
$\lambda_C$ : radiation wavelength
$f_D$ : Doppler shift frequency
$f_{PRF}$ : pulse repetition frequency
$\psi_c$ : clutter ring grazing angle (shown positive in Figure 2-1)
$r_c$ : range to clutter ring
$\Delta r$ : clutter patch range extent
$\Delta\phi$ : clutter patch angular extent
$\rho_r$ : radar range resolution
$N_c$ : number of clutter patches in the clutter ring
$r_E$ : effective mean radius of the Earth

*Table 2-1. Physical, scenario, system, and simulation parameters, and key relations for a clutter patch.*

In most surveillance array systems the narrow bandwidth criterion is satisfied, and it is assumed to be true for the cases considered herein. For a J-element linear array with inter-element spacing d, the narrow bandwidth criterion can be expressed as (Hudson, 1981)

$$(J-1)d << \frac{\nu}{f_{BBW}} \qquad \text{Narrow Bandwidth Criterion} \tag{2-1}$$

where $\nu$ (lower case greek nu) denotes the speed of propagation of the electromagnetic wave and $f_{BBW}$ is the one-sided amplitude waveform (baseband) bandwidth. In this work the inter-element spacing d is selected as (see Table 2-1)

$$d = \frac{\lambda_C}{2} \tag{2-2}$$

This choice of inter-element spacing avoids the generation of more than one array antenna beam, the so-called grating lobes (Monzingo and Miller, 1980; Skolnik, 1970). Many practical radar array systems are designed with $d \leq 0.5\,\lambda_C$, which also results in one beam. An equivalent expression for the narrow bandwidth criterion is obtained by substituting Equation (2-2) into Equation (2-1),

$$J-1 << \frac{2f_C}{f_{BBW}} \qquad \text{Narrow Bandwidth Criterion} \tag{2-3}$$

This criterion may not be met for arrays with a large number of elements and/or a large amplitude waveform bandwidth.

The elevation dimension is included to first-order in this formulation. This approximation is reasonable for long-range surveillance radar, and suffices for the purposes of this program. A more complete model includes a planar (two-dimensional) array

with main beam elevation steering. However, the model adopted herein can be used to represent the cases where the channels correspond to antenna subarrays in either one or both dimensions (azimuth and elevation); that is, the channels are J subsets of appropriately-combined individual elements. In particular, the clutter component model includes the cases wherein $J_e$ elevation channels are beamformed into a single row.

Consider the output of the ith channel corresponding to a single range resolution cell after pulse compression, demodulation down to baseband, and temporal sampling. Notice that for a single range resolution cell, each channel output includes the return from multiple ground clutter rings (the primary range ring as well as ambiguous range rings). Denote this complex-valued, discrete-time waveform as $\{x_i(n) \mid n = 0, 1, \ldots, N\text{-}1\} = \{x_i(n)\}$. Specifically, for a single range resolution cell and one CPI, the ith channel output is

$$x_i(n) = s_i(n) + i_i(n) + c_i(n) + w_i(n) \qquad 0 \le n \le N - 1 \tag{2-4}$$

where n is an integer denoting the sampling time instant, $\{s_i(n)\}$ denotes the signal (moving target) return at the ith channel, $\{i_i(n)\}$ denotes the total broadband interference (jamming) received at the ith channel, $\{c_i(n)\}$ denotes the total ground clutter return at the ith channel, and $\{w_i(n)\}$ denotes the combination of all the statistically-independent noise sources in the ith channel. Array receiver noise is usually the dominant noise contributor to $\{w_i(n)\}$, and that is assumed to be true for the model considered herein. Each of the output components is assumed to be a stationary, ergodic, zero-mean, Gaussian-distributed random process.

The temporal sampling interval $\Delta t$ for the channel output waveform is the pulse repetition interval (PRI) $T_I$, which is the inverse of the PRF. Thus, it is more appropriate to express the function argument in Equation (2-4) as $nT_I$, instead of n. However,

a PRF-normalized frequency variable is used in the formulation developed below, and such normalization is equivalent to normalization of the sampling interval by the PRI. As a result, the sampling interval $\Delta t$ associated with the variable $n$ (or with the variable $m$, which is used herein to denote correlation lags), can be assumed to be equal to unity and dimensionless. Also, the initial time of the CPI is taken as $n = 0$ without loss of generality since the process is stationary.

Let channel 1 be the temporal and spatial reference for the array. For a uniform linear array the waveforms from the $J$ channels can be concatenated into the following vectors,

$$\underline{x}(n) = \underline{s}(n) + \underline{i}(n) + \underline{c}(n) + \underline{w}(n) \qquad 0 \le n \le N-1 \tag{2-5}$$

$$\underline{x}(n) = \begin{bmatrix} x_1(n) \\ x_2(n) \\ \vdots \\ x_J(n) \end{bmatrix} \tag{2-6}$$

$$\underline{s}(n) = \begin{bmatrix} s_1(n) \\ s_2(n) \\ \vdots \\ s_J(n) \end{bmatrix} = \begin{bmatrix} s_1(n) \\ s_1(n+\tau) \\ \vdots \\ s_1(n+\kappa\tau) \end{bmatrix} \tag{2-7}$$

$$\underline{i}(n) = \begin{bmatrix} i_1(n) \\ i_2(n) \\ \vdots \\ i_J(n) \end{bmatrix} = \begin{bmatrix} i_1(n) \\ i_1(n+\tau) \\ \vdots \\ i_1(n+\kappa\tau) \end{bmatrix} \tag{2-8}$$

$$(2\text{-}9) \qquad \underline{c}(n) = \begin{bmatrix} c_1(n) \\ c_2(n) \\ \vdots \\ c_J(n) \end{bmatrix} = \begin{bmatrix} c_1(n) \\ c_1(n+\tau) \\ \vdots \\ c_1(n+\kappa\tau) \end{bmatrix}$$

$$(2\text{-}10) \qquad \underline{w}(n) = \begin{bmatrix} w_1(n) \\ w_2(n) \\ \vdots \\ w_J(n) \end{bmatrix}$$

with $\kappa = J - 1$ in order to simplify notation, and where $\tau$ is the inter-element time advance (with respect to channel 1, the reference channel). For a range resolution cell at azimuth angle $\phi$ and elevation angle $\theta$, the inter-element time advance is obtained from the geometry established in Figure 2-1 as

$$(2\text{-}11) \qquad \tau = \frac{d}{v}\cos(\theta)\sin(\phi) = \frac{d}{\lambda_C f_C}\cos(\theta)\sin(\phi)$$

where all variables are as defined previously (see Table 2-1).

As indicated in Equations (2-7)-(2-9), the kth element of each of the signal, interference, and clutter components, is an advanced version of the scalar waveform in channel 1, with $\tau$ as the inter-element advance. This follows from the assumptions and conventions established above. Array noise, however, is assumed to be uncorrelated from channel to channel, and with the same power in each channel (the equal power assumption can be relaxed easily, but it is representative of realistic conditions). These characteristics determine the structure of the covariance matrix sequence of each component.

## 2.2 Signal (Moving Target) True Covariance Model

The signal (moving target) component at the output of the kth channel, $\{s_k(n)\}$, is the radar return from each moving target located within the range resolution cell of interest. Consider a target moving towards the radar array with a constant velocity $V_t$ along a trajectory aligned with azimuth angle $\phi_t$ and elevation angle $\theta_t$. The target's radial velocity is defined to be positive when the target is moving towards the radar, and negative otherwise. Such a target has a normalized Doppler frequency shift $f_{td}$ of the form (Figure 2-1 and Table 2-1)

$$f_{td} = \frac{f_{tD}}{f_{PRF}} = \frac{2\left[V_t + V_p \cos(\theta_t)\sin(\phi_t - \gamma)\right]}{f_{PRF}\lambda_C} \tag{2-12}$$

where $f_{tD}$ is the normalized target Doppler frequency shift, and the PRF provides the normalization. This normalized Doppler frequency assumes unambiguous values in the range $-0.5 \le f_d < 0.5$.

From the definition of spatial frequency in Table 2-1 and the geometry depicted in Figure 2-1, the target's dimensionless spatial frequency $f_{ts}$ is of the form

$$f_{ts} = f_C\tau = \frac{d}{\lambda_C}\cos(\theta_t)\sin(\phi_t) \tag{2-13}$$

where the inter-element time advance $\tau$ is as defined in Equation (2-11). Adopting the half-wavelength value for $d$ (see Equation (2-2)), the target's spatial frequency becomes

$$f_{ts} = 0.5\cos(\theta_t)\sin(\phi_t) \qquad -90° \le \theta_t \le 90°;\ -90° \le \phi_t \le 90° \tag{2-14}$$

Given the allowable range of values for the azimuth and elevation angles, it follows that $-0.5 \le f_{ts} \le 0.5$. Notice that the sign of the

azimuth angle determines the sign of the spatial frequency. For the geometry, conventions, and definitions established in Figure 2-1, Table 2-1, and above, the return from a target illuminated by the main beam at a positive azimuth angle has a positive spatial frequency $f_{ts}$.

Moving targets are modeled as the output sequence of a linear, stationary, discrete-time, complex-valued, stochastic system in state-space form. Specifically, for the case of $G_s$ targets, the model adopted herein is

(2-15a) $$\underline{y}(n+1) = F\underline{y}(n) + \underline{u}(n) \qquad n \geq 0$$

(2-15b) $$\underline{s}(n) = H^H \underline{y}(n) \qquad n \geq 0$$

(2-15c) $$E[\underline{y}(0)] = \underline{0}$$

(2-15d) $$E[\underline{y}(0)\underline{y}^H(0)] = P(0) = P$$

(2-15e) $$E[\underline{y}(n)\underline{y}^H(n)] = P(n)$$

where $\underline{y}(n)$ is the $G_s$-dimensional state vector, with $\underline{y}(0)$ Gaussian-distributed and zero-mean; $\underline{u}(n)$ is the $G_s$-dimensional input vector; and $\underline{s}(n)$ is the $G_s$-dimensional output vector. The input sequence $\{\underline{u}(n)\}$ is Gaussian-distributed with mean zero and covariance matrix

(2-16) $$E[\underline{u}(n)\underline{u}^H(n)] = Q$$

It follows that the state and output sequences are both Gaussian-distributed with mean zero also. Matrix $F$ is the $G_s x G_s$ system matrix, which defines the time evolution of the process. Matrix $H$ is the $G_s x J$ output distribution matrix, $P(n)$ is the state covariance matrix at time $n$, and $P$ is the state covariance matrix

at steady-state. For a system of the type (2-15), stationarity implies asymptotic stability, which in turn implies that steady-state conditions are attained at a finite time. The system matrix, output matrix, input covariance matrix, and state covariance matrix are defined as follows:

(2-17a) $$F = \begin{bmatrix} F(1,1) & 0 & \cdots & 0 \\ 0 & F(2,2) & \cdots & 0 \\ \vdots & \vdots & \ddots & \vdots \\ 0 & 0 & \cdots & F(G_s,G_s) \end{bmatrix}$$

(2-17b) $$F(k,k) = F_k = a_k \exp(j2\pi f_{tdk}) \qquad k = 1, 2, \ldots, G_s$$

(2-17c) $$0 \le a_k < 1 \qquad k = 1, 2, \ldots, G_s$$

(2-18a) $$H^H = \left[ \underline{e}_J(f_{ts1}) \;\; \underline{e}_J(f_{ts2}) \;\; \cdots \;\; \underline{e}_J(f_{tsG_s}) \right]$$

(2-18b) $$\underline{e}_J(f_{ts}) = \begin{bmatrix} 1 \\ e^{j2\pi f_{ts}} \\ \vdots \\ e^{j2\pi f_{ts}\kappa} \end{bmatrix}$$

(2-18c) $$\kappa = J - 1$$

(2-19a) $$Q = \begin{bmatrix} Q(1,1) & 0 & \cdots & 0 \\ 0 & Q(2,2) & \cdots & 0 \\ \vdots & \vdots & \ddots & \vdots \\ 0 & 0 & \cdots & Q(G_s,G_s) \end{bmatrix}$$

(2-19b) $$Q(k,k) = Q_k = (1 - a_k^2)\, P_k = (1 - a_k^2)\, \sigma_{sk}^2 \qquad k = 1, 2, \ldots, G_s$$

(2-20) $$P(n) \Rightarrow P \qquad \text{as} \qquad n \Rightarrow \infty$$

$$(2\text{-}21) \qquad P = \begin{bmatrix} P_1 & 0 & \cdots & 0 \\ 0 & P_2 & \cdots & 0 \\ \vdots & \vdots & \ddots & \vdots \\ 0 & 0 & \cdots & P_{G_s} \end{bmatrix} = \begin{bmatrix} \sigma_{s1}^2 & 0 & \cdots & 0 \\ 0 & \sigma_{s2}^2 & \cdots & 0 \\ \vdots & \vdots & \ddots & \vdots \\ 0 & 0 & \cdots & \sigma_{sG_s}^2 \end{bmatrix}$$

Selection of the initial state covariance matrix as a diagonal matrix equal to the steady-state covariance (see Equation (2-15d)) results in the straightforward calculation of the the input noise covariance (Equation (2-19b)), and simplifies data generation (Section 2.7). Furthermore, each target can be assigned a different power since the diagonal elements of $P$ can be distinct from each other. This allows assignation of a distinct signal-to-noise ratio (SNR) to each target.

This model has several features of interest. First, the temporal evolution of the kth target is represented by the kth state exclusively via the damping coefficient, $a_k$, and the target's normalized Doppler shift frequency, $f_{tdk}$. Second, the system is exponentially stable because all the coefficients $a_k$ are less than unity, as defined in Equation (2-17c). As a consequence, the stochastic identification algorithms of interest in this program can be applied without concern for pathological behaviour. Third, the spatial structure is assigned via the columns of $H^H$, separately from the temporal structure. The columns of $H^H$ defined in Equation (2-18b) are referred to as spatial frequency vectors, where $f_{tsk}$ is the spatial frequency of the kth target. Fourth, the power of the kth moving target is $P_k = \sigma_{sk}^2$, and this power is contributed to each channel. As a result, the total signal power in each channel is equal to the sum of the diagonal of $P$. Fifth, the covariance matrix sequence of the output is determined in closed form as a function of the system parameters defined above. Specifically, let $\{R_{ss}(m)\}$ denote the JxJ auto-covariance matrix sequence for the zero-mean process $\{\underline{s}(n)\}$, then

$$(2\text{-}22) \qquad R_{ss}(m) = E[\underline{s}(n)\underline{s}^H(n-m)] = H^H F^m P H \qquad m \geq 0$$

with negative lags defined as

$$(2\text{-}23) \qquad R_{ss}(-m) = E[\underline{s}(n)\underline{s}^H(n+m)] = R_{ss}^H(m) \qquad m \geq 0$$

Equations (2-22) and (2-23) define the true covariance matrix sequence, $\{R_{ss}(m)\}$. Matrix $R_{ss}(m)$ is Hermitian only for $m = 0$; however, matrix $R_{ss}(m)$ has Toeplitz structure for all $m$ due to the spatially-induced relationship among the elements of $\underline{s}(n)$, as expressed in Equation (2-7).

Equation (2-22) can be used to generate the true covariance matrix sequence directly. However, due to the special structure of matrices F, H, and P, the right-hand-side of Equation (2-22) can be expressed in a form that requires less computations. Namely, the $m$th lag covariance matrix can be expressed as

$$(2\text{-}24) \qquad R_{ss}(m) = \sum_{k=1}^{G_s} a_k^m \, e^{j2\pi m f_{tdk}} \, P_k \, \underline{e}_J(f_{tsk}) \, \underline{e}_J^H(f_{tsk}) \qquad m \geq 0$$

Equation (2-24) requires less computations than Equation (2-22). However, given the structure of the spatial frequency vectors, the form of Equation (2-24), and the fact that matrix $R_{ss}(m)$ is Toeplitz, a simpler approach can be defined to generate the true matrix covariance sequence, as described next. First compute the following two J-dimensional vectors,

$$(2\text{-}25) \qquad \underline{e}_c(m) = \sum_{k=1}^{G_s} a_k^m \, e^{j2\pi m f_{tdk}} \, \sigma_{sk}^2 \, \underline{e}_J(f_{tsk}) \qquad m \geq 0$$

$$(2\text{-}26) \qquad \underline{e}_r^H(m) = \sum_{k=1}^{G_s} a_k^m \, e^{j2\pi m f_{tdk}} \, \sigma_{sk}^2 \, \underline{e}_J^H(f_{tsk}) \qquad m \geq 0$$

Notice that $\underline{e}_c(m)$ is a column vector, whereas $\underline{e}_r^H(m)$ is a row vector. Then, for each desired value of $m$, matrix $R_{ss}(m)$ is formed as follows: (a) set the first column of $R_{ss}(m)$ equal to vector $\underline{e}_c(m)$, which defines the main diagonal and all the diagonals below the main diagonal; and (b) set the first row of $R_{ss}(m)$ equal to vector $\underline{e}_r^H(m)$, which defines the main diagonal and all the diagonals above the main diagonal. There is no conflict along the main diagonal because the first element of $\underline{e}_c(m)$ is the same as the first element of $\underline{e}_r^H(m)$.

## 2.3 Broadband Interference (Jamming) True Covariance Model

The broadband interference (jamming) at the output of the $k$th channel, $\{i_k(n)\}$, represents the received interference from all direct jamming sources. Jammer multipath and distributed jammers are not included in the model at the present time. Consider a jamming point source located at azimuth angle $\phi_i$, as shown in Figure 2-1 for a negative-valued angle case, and elevation angle $\theta_i$ (not shown in Figure 2-1). This interference is modeled at the output of the each channel as a Gaussian-distributed, zero-mean, white sequence with variance $\sigma_i^2$. The spatial variation of this component is described by the dimensionless spatial frequency $f_{is}$, which is given as

$$(2\text{-}27) \qquad f_{is} = f_C \tau = \frac{d}{\lambda_C} \cos(\theta_i) \sin(\phi_i) = 0.5 \cos(\theta_i) \sin(\phi_i)$$

where the inter-element time advance $\tau$ is as defined in Equation (2-11), and the half-wavelength inter-element spacing assumption

(Equation (2-2)) has been applied. Each channel receives the same amount of power from this jammer.

The true covariance matrix sequence $\{R_{ii}(m)\}$ for $G_i$ interference sources as described above is given as

$$(2\text{-}28a) \qquad R_{ii}(0) = E[\underline{i}(n)\,\underline{i}^H(n\text{-}m)] = \sum_{k=1}^{G_i} \sigma_{ik}^2\, \underline{e}_J(f_{isk})\, \underline{e}_J^H(f_{isk})$$

$$(2\text{-}28b) \qquad R_{ii}(m) = E[\underline{i}(n)\underline{i}^H(n\text{-}m)] = [0] \qquad m \neq 0$$

where $\underline{e}_J(f_{isk})$ is the spatial frequency vector for the kth jamming source at the spatial frequency $f_{isk}$, and $\sigma_{ik}^2$ is the variance (power) of the kth jamming source. Each channel receives the same amount of power from this jammer. Notice that Equation (2-28a) is of the same form as Equation (2-24) for $m = 0$. Thus, matrix $R_{ii}(0)$ is Toeplitz. Also, the generation of $R_{ii}(0)$ can be carried out via the same procedure used to generate $R_{ss}(0)$.

## 2.4 Receiver Array Noise True Covariance Model

The receiver array noise at the output of the kth channel, $\{w_k(n)\}$, represents all noise sources that arise within the kth channel. This component is modeled as a Gaussian-distributed, zero-mean, white sequence with variance (power) $\sigma_{nk}^2$, and uncorrelated from channel to channel. Thus, the spatial variation is broadband also. It follows that the true covariance matrix sequence $\{R_{ww}(m)\}$ for this output component is given as

$$(2\text{-}29a) \qquad R_{ww}(0) = E[\underline{w}(n)\,\underline{w}^H(n)] = \begin{bmatrix} \sigma_{n1}^2 & 0 & \cdots & 0 \\ 0 & \sigma_{n2}^2 & \cdots & 0 \\ \vdots & \vdots & \ddots & \vdots \\ 0 & 0 & \cdots & \sigma_{nJ}^2 \end{bmatrix}$$

(2-29b) $R_{ww}(m) = E[\underline{w}(n)\,\underline{w}^H(n-m)] = [0]$ $\quad m \neq 0$

Notice that the covariance matrix $R_{ww}(0)$ as defined in Equation (2-29a) is not Toeplitz. This general model is applicable in some cases, specially when each channel corresponds to a different type of sensor. However, in the surveillance radar case considered here it is appropriate to assign the same variance to the noise in each channel. Thus, the model adopted herein for the receiver array noise true covariance matrix sequence $\{R_{ww}(m)\}$ is

(2-30a) $R_{ww}(0) = E[\underline{w}(n)\,\underline{w}^H(n)] = \sigma_n^2\, I_J$

(2-30b) $R_{ww}(m) = E[\underline{w}(n)\,\underline{w}^H(n-m)] = [0]$ $\quad m \neq 0$

with $\sigma_n^2$ the noise sequence variance (power) in each channel. Matrix $R_{ww}(0)$ in Equation (2-30a) is Toeplitz. Notice that the difference between the noise covariance $R_{ww}(0)$ and the interference covariance $R_{ii}(0)$ is the spatial correlation present in $R_{ii}(0)$. This difference is sufficient for adaptive cancelation algorithms to distinguish between noise and interference.

## 2.5 Ground Clutter True Covariance Model

The ground clutter component at the output of the kth channel, $\{c_k(n)\}$, is the combination of the radar return from all ground patches irradiated by the transmitted pulse sequence. This includes the return from ground patches in the primary range ring (see Figure 2-1), which is irradiated by the array main beam as well as by the sidelobes; also included is the return from range rings at ambiguous ranges and from ranges illuminated by the elevation pattern sidelobes. Since each range ring extends over all azimuth angles, ground clutter return exhibits power in a continuum of Doppler and spatial frequencies. In fact, a typical

ground clutter power spectrum (see, for example, Jaffer et al., 1991) exhibits a "ridge" in the two-dimensional (2-D) frequency plane, as indicated in Figure 2-2. In cases where the crab angle is zero, the clutter ridge occurs along a straight line that passes through the origin of the 2-D frequency plane, as in Figure 2-2. When the crab angle is non-zero, the trace defined by the ridge is a nonlinear function of various system and scenario parameters. The number of clutter ridges is doubled when array backlobes are significant and the crab angle is non-zero (Ward, 1994). The model defined herein accounts for sidelobe clutter and backlobe clutter, but does not include ambiguous range rings nor does it include clutter from elevation pattern sidelobes.

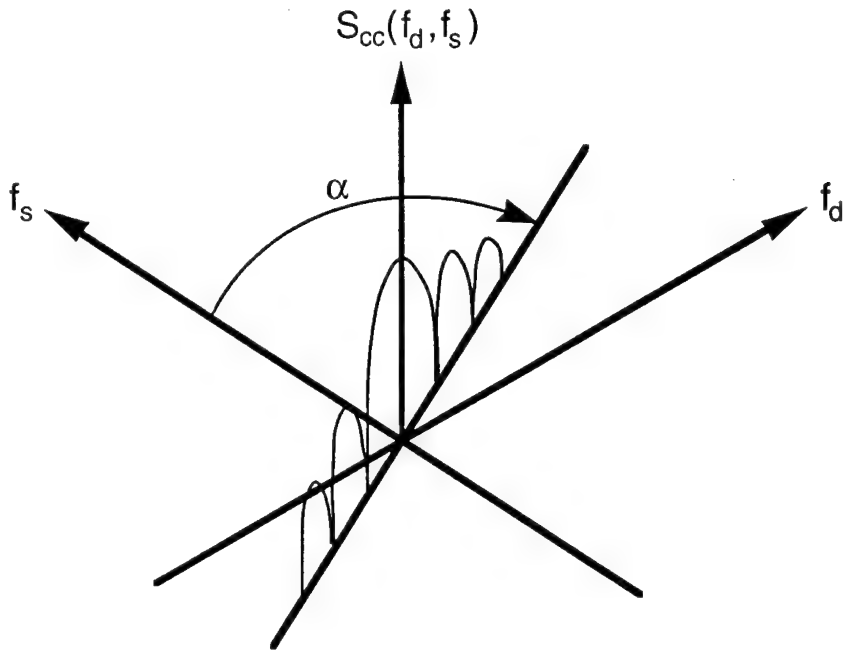


*Figure 2-2. Two-dimensional clutter spectrum and angle* $\alpha$.

The clutter ridge angle $\alpha$ (see Figure 2-2) is defined as (Jaffer et al., 1991; Ward, 1994)

$$\alpha = \tan^{-1}\left[\frac{4V_p}{f_{PRF}\lambda_C}\right] = \tan^{-1}[\upsilon] \tag{2-31}$$

$$\upsilon = \frac{4V_p}{f_{PRF}\lambda_C} \tag{2-32}$$

where $\upsilon$ (the Greek letter upsilon) is the slope of the clutter ridge (Table 2-1). When $\upsilon > 1$ the clutter spectrum has ambiguities (components at normalized Doppler frequencies greater than 0.5), and, consequently, the clutter Doppler spectrum aliases into the unambiguous Doppler space, $-0.5 \leq f_d < 0.5$ (Ward, 1994). This condition is manifested in the 2-D frequency-domain plane as multiple ridges (straight lines) of different length. If the crab angle is non-zero, the straight-lined ridges become curved.

The ground clutter model described herein is based on the analytic model proposed by Jaffer et al. (1991), and also adopted recently by Ward (1994). However, the notation used herein follows Ward (1994) more closely. Two non-trivial simplifications to these models are introduced herein: (a) only a single range ring is modeled, and (b) intrinsic clutter motion is not modeled. In Ward's formulation the clutter return from a range ring is determined by $N_c$ equal-area patches, and each patch consists of a single, complex-valued scatterer with mean zero and Rayleigh-distributed magnitude. Furthermore, the scatterers are assumed to be pairwise statistically independent. Ward's model for the true covariance sequence and for data generation are based on an expression for clutter-to-noise ratio (CNR) as a function of azimuth, at a fixed elevation angle. Specifically, for a single clutter ring Ward's CNR as a function of azimuth and elevation is of the form

$$\xi_c(\phi,\theta) = \frac{P_t\, T_u\, \lambda_C^2\, \zeta_c\, G_{cr}\, G_t(\phi,\theta)\, g_r(\phi,\theta)}{(4\pi)^3\, N_o\, L_s\, r_c^4} \tag{2-33}$$

where $P_t$ denotes the peak transmitted power, $T_u$ denotes the uncompressed pulse duration, $\lambda_C$ denotes the radiation wavelength, $\zeta_c$ denotes the clutter patch radar cross section (RCS), $G_{cr}$ denotes the receive column pattern (beamforming) gain, $G_t(\phi,\theta)$ denotes the transmit antenna power pattern as a function of azimuth and elevation, $g_r(\phi,\theta)$ denotes the receive element antenna power pattern as a function of azimuth and elevation, $N_o$ denotes the receiver noise power spectral density, $L_s$ denotes the system losses, and $r_c$ denotes the range from the platform to the clutter ring illuminated by the mainbeam. Parameters $P_t$, $T_u$, $L_s$, and $r_c$ are radar system and scenario parameters provided as inputs to the software; the remaining parameters are calculated as described next. Pre-specified physical constants are listed in Table 2-2.

The radiation wavelength is determined given the speed of light, $v$, and the radiation frequency, $f_C$, as

$$\lambda_C = \frac{v}{f_C} \tag{2-34}$$

For $v$ in km/sec and $f_C$ in MHz, the wavelength is calculated in mm. And the receiver noise power spectral density is defined as (Skolnik, 1980)

$$N_o = k_B\, T_o\, F_n \tag{2-35}$$

where $F_n$ is the system noise figure, a radar system parameter provided as input to the software. Boltzmann's constant, $k_B$, and the standard temperature, $T_o$, are as specified in Table 2-2.

| SYMBOL | DESCRIPTION | VALUE |
|---|---|---|
| $v$ | Speed of light | $2.998 \times 10^5$ km/sec |
| $r_o$ | Mean radius of theEarth | 6,368.0 km |
| $r_E$ | Effective radius of the Earth (= (4/3) $r_o$) | 8,490.66667 km |
| $k_B$ | Boltzmann's constant | $1.38 \times 10^{-23}$ W/(Hz-K) |
| $T_o$ | Standard temperature for radar system | 290 K |
| $\gamma_c$ | Constant-gamma clutter reflectivity model parameter for heavy land clutter case | -3 dB |

*Table 2-2. Physical constants for multichannel signal model.*

The clutter patch RCS, $\zeta_c$, is determined as

(2-36) $$\zeta_c = s_o A_c = s_o W_c L_c$$

where $s_o$ is the clutter patch reflectivity, $A_c$ is the clutter patch area, $W_c$ is the clutter patch width, and $L_c$ is the clutter patch length. Clutter patch reflectivity is determined according to the constant-gamma model, which is defined as (Nathanson, 1991)

(2-37) $$s_o = \gamma_c \sin(\psi_c)$$

with the reflectivity model parameter $\gamma_c$ as specified in Table 2-2, and the clutter ring grazing angle $\psi_c$ as defined in Figure 2-1 and

Table 2-1. For each patch in the 360 deg clutter ring, clutter patch width is calculated as

$$W_c = r_c \Delta\phi = r_c \frac{2\pi}{N_c} \tag{2-38}$$

with the range to clutter ring $r_c$ as defined in Figure 2-1, and the clutter patch angular extent $\Delta\phi$ as defined in Table 2-1. Also, $N_c$ is the number of clutter patches in the clutter ring (Table 2-1). Likewise, each patch in the 360 deg clutter ring is of length $L_c$, calculated as

$$L_c = \begin{cases} \dfrac{\rho_r}{\cos(\psi_c)} = \dfrac{v}{2 f_B \cos(\psi_c)} & \text{if} \quad \rho_r \tan(\psi_c) \le r_c \tan(\beta_{1e}) \\ \dfrac{2 r_c \tan\left(\dfrac{\beta_{1e}}{2}\right)}{\sin(\psi_c)} & \text{if} \quad \rho_r \tan(\psi_c) > r_c \tan(\beta_{1e}) \end{cases} \tag{2-39}$$

with $\rho_r$ denoting the radar range resolution, $f_B$ denoting the receiver bandwidth, $\beta_{1e}$ denoting the transmit array one-way, 3-dB elevation beamwidth, and the other parameters are as defined previously. The receiver bandwidth is a radar system parameter provided as input to the software; whereas the elevation beamwidth is approximated as (Skolnik, 1970)

$$\beta_{1e} = \frac{b_w \lambda_C}{(J_e - 1) d \cos(\theta_0)} \qquad \theta_0 < 60° \tag{2-40a}$$

$$\beta_{1e} = 1.24 \sqrt{\frac{\lambda_C}{(J_e - 1) d}} \qquad \theta_0 = 90° \tag{2-40b}$$

$$(2\text{-}40c) \qquad b_w = \begin{cases} 0.866 & \text{for uniform taper} \\ 1.3 & \text{for Dolph–Chebyshev taper} \end{cases}$$

where $J_e$ is the number of elevation axis elements beamformed into one azimuth channel, $d$ is the linear array inter-element spacing (assumed to be the same for elevation and azimuth), $\theta_0$ is the clutter ring elevation angle calculated as in Table 2-2, and $b_w$ is a constant factor. Azimuth angle and inter-element spacing are illustrated in Figure 2-1. The cosine factor in Equation (2-40a) accounts for scanning-induced broadening of the main beam (Skolnik, 1970). The constant factor in Equation (2-40a) is introduced herein to account for taper-induced beam broadening. Its minimum value is 0.866 for the uniform taper, as indicated in Equation (2-40c). The value set in Equation (2-40c) for Dolph-Chebyshev tapering is a representative value. An expression for the exact value is unknown since the beam broadening induced by the Dolph-Chebyshev taper is a complicated function of sidelobe level and number of elements. Other elevation pattern tapers applied to reduce the antenna sidelobes also result in a broader beamwidth (with respect to the uniform taper).

The 2-D transmit array has an antenna power pattern denoted as $G_t(\phi,\theta)$. For simplicity, the elevation dimension is ignored herein, and the clutter return is calculated for the mainbeam elevation ($\theta_0$) only. Thus, the antenna power pattern used to generate the ground clutter model is $G_t(\phi,\theta_0)$. From standard array theory, the antenna pattern is the product of the element pattern and the array pattern (Skolnik, 1980). Let $g_e(\phi,\theta_0)$ denote the element power pattern, which is assumed to be a squared cosine in the azimuth axis,

$$(2\text{-}41) \qquad g_e(\phi,\theta_0) = \begin{cases} \cos^2(\phi) & \text{for} \quad -90° \le \phi < 90° \\ G_b \cos^2(\phi) & \text{for} \quad 90° \le \phi < 270° \end{cases}$$

where $G_b$ is the backlobe region attenuation. This element pattern model is used by Ward (1994). Now let $G_a(\phi,\theta_0)$ denote the array pattern in the azimuth axis, which is assumed to be either uniform or Dolph-Chebyshev. Other pattern options can be added to the model in the future. The uniform array pattern is generated as (Skolnik, 1980)

$$(2\text{-}42) \qquad G_a(\phi,\theta_0) = \begin{cases} \left| \dfrac{\sin\left( \dfrac{J\pi d}{\lambda_C} \left\{ \sin(\phi) - \sin(\phi_0) \right\} \right)}{J \sin\left( \dfrac{\pi d}{\lambda_C} \left\{ \sin(\phi) - \sin(\phi_0) \right\} \right)} \right|^2 & \text{for} \quad -90° \le \phi < 90° \\ G_b \left| \dfrac{\sin\left( \dfrac{J\pi d}{\lambda_C} \left\{ \sin(\phi) - \sin(\phi_0) \right\} \right)}{J \sin\left( \dfrac{\pi d}{\lambda_C} \left\{ \sin(\phi) - \sin(\phi_0) \right\} \right)} \right|^2 & \text{for} \quad 90° \le \phi < 270° \end{cases}$$

where $\phi_0$ is the mainbeam azimuth angle (see Figure 2-1 and Table 2-1); and the Dolph-Chebyshev array pattern (characterized by equi-level sidelobes) is generated as

$$(2\text{-}43a) \qquad G_a(\phi,\theta_0) = \begin{cases} \dfrac{1}{U} \left| F\left[ \underline{e}_J(f_{s0}) \otimes \underline{u} \right] \right|^2 & \text{for} \quad -90° \le \phi < 90° \\ G_b \dfrac{1}{U} \left| F\left[ \underline{e}_J(f_{s0}) \otimes \underline{u} \right] \right|^2 & \text{for} \quad 90° \le \phi < 270° \end{cases}$$

(2-43b) $$\underline{e}_J(f_{s0}) = \begin{bmatrix} 1 \\ e^{j2\pi f_{s0}} \\ \vdots \\ e^{j2\pi f_{s0}\kappa} \end{bmatrix}$$

(2-44c) $$f_{s0} = \frac{d}{\lambda_C}\cos(\theta_0)\sin(\phi_0)$$

here $\underline{u}$ is the J-dimensional vector of Dolph-Chebyshev weights, $\mathbf{F}$ denotes the discrete Fourier transform (DFT) operator, and $\otimes$ denotes the Schur (element-by-element) product. The Dolph-Chebyshev weights are calculated as in (Urkowitz et al., 1973), which requires specification of the number of weights (dimension of the vector $\underline{u}$) and the desired sidelobe level. The spatial frequency vector $\underline{e}_J(f_{s0})$ steers the array pattern main beam to the desired azimuth and elevation, and the real-valued, scalar $U$ is a normalization factor selected so that $G_a(\phi_0,\theta_0) = 1$. Given these definitions, the transmit antenna power pattern is obtained as

(2-45) $$G_t(\phi,\theta_0) = G_o\, G_a(\phi,\theta_0)\, g_e(\phi,\theta_0)$$

where $G_o$ is the transmit pattern gain. The gain $G_o$ is a radar system parameter provided as input to the software.

As assumed for the transmit pattern, the elevation dimension is ignored herein for the receive element antenna power pattern, $g_r(\phi,\theta_0)$, and the clutter return is calculated for the mainbeam elevation ($\theta = \theta_0$) only. Thus, the receive element antenna power pattern is obtained as

(2-46) $$g_r(\phi,\theta_0) = g_e(\phi,\theta_0)$$

This model is adopted for the case of a linear receive array, as well as for the case of a 2-D receive array with beamforming in the elevation axis (since the azimuth axis is unchanged).

The receive column pattern beamforming gain, $G_{cr}$, is included in the CNR model to account for the cases where the receive array is a 2-D (multi-column, multi-row) array of elements that is "collapsed" into a linear (single-row) array by beamforming in the elevation (column) axis. Therefore, this gain is computed as

$$G_{cr} = J_e \, G_e \tag{2-47}$$

where $J_e$ is the number of elevation axis elements beamformed into one azimuth channel, and $G_e$ is the receive element gain. Notice that for $J_e = 1$ the product $G_{cr}\, g_r(\phi,\theta_0) = G_e\, g_e(\phi,\theta_0)$ and represents a single receive element, as should be the case. Both constants $J_e$ and $G_e$ are radar system parameters provided as inputs to the software. This completes the CNR model definition.

Consider now the vector spatio-temporal ground clutter process, $\{\underline{c}(n)\}$, as defined in Equation (2-9). This vector process is modeled herein as the sum of the return from all the clutter patches in the clutter ring illuminated by the mainbeam. That is,

$$c_{k+1}(n) = \sum_{p=0}^{N_c-1} \eta_p \, e^{j2\pi f_{cdp} n} \, e^{j2\pi f_{csp} k} \qquad \begin{matrix} n = 0, 1, \ldots, N-1 \\ k = 0, 1, \ldots, J-1 \end{matrix} \tag{2-48a}$$

$$\underline{c}(n) = \sum_{p=0}^{N_c-1} \eta_p \, e^{j2\pi f_{cdp} n} \, \underline{e}_J\left(f_{csp}\right) \qquad n = 0, 1, \ldots, N-1 \tag{2-48b}$$

where $\eta_p$ denotes the complex-valued clutter return from the single scatterer representing the pth patch, and $f_{cdp}$ and $f_{csp}$ denote the

normalized Doppler frequency and spatial frequency, respectively, of the pth clutter patch. These frequencies are computed as

(2-49) $$f_{cdp} = 0.5\, \upsilon \cos(\theta_0) \sin(\phi_p - \gamma)$$

(2-50) $$f_{csp} = (d/\lambda_C) \cos(\theta_0) \sin(\phi_p) = 0.5 \cos(\theta_0) \sin(\phi_p)$$

(2-51) $$\phi_p = -\pi + p\,\Delta\phi \qquad p = 0, 1, \ldots, N_c - 1$$

with $\upsilon$ the clutter ridge slope as defined in Equation (2-32); also, $\Delta\phi$ is the clutter patch angular extent, and $N_c$ is the number of clutter patches in a clutter ring (see Figure 2-1 and Table 2-1). $N_c$ is a scenario parameter, and is provided as input to the software. Notice that the clutter patch spatial frequencies are bounded by ±0.5; in contrast, the clutter patch Doppler frequencies are unbounded. As discussed earlier, Doppler frequencies greater than 0.5 or smaller than -0.5 are ambiguous, and these frequencies fold over onto the observable frequency range, $-0.5 \le f_d < 0.5$.

The clutter return from the single scatterer representing the pth patch is modeled herein as a complex-valued, scalar random variable with mean zero and Gaussian-distributed real and imaginary parts (Rayleigh-distributed magnitude). Also, all clutter patches are assumed to be pairwise statistically independent. It follows from the definition of CNR that the power (variance) of the pth patch clutter return, $\sigma_{cp}^2$, is obtained as

(2-52) $$E\left[\eta_p \eta_q^*\right] = \sigma_{cp}^2\, \delta_{p-q} = \sigma_n^2\, \xi_c\left(\phi_p, \theta_0\right) \delta_{p-q} \qquad -\pi \le \phi_p < 1.5\pi$$

where $\delta_{p-q}$ is the Kronecker delta, which is defined as

$$\delta_{p-q} = \begin{cases} 1 & \text{if} \quad p = q \\ 0 & \text{otherwise} \end{cases} \tag{2-53}$$

The receiver noise variance, $\sigma_n^2$, is a radar system parameter, and is provided as input to the software. With these definitions, the clutter true auto-covariance matrix sequence $\{R_{cc}(m)\}$ is obtained as

$$R_{cc}(m) = E\left[\underline{c}(n)\,\underline{c}^H(n-m)\right] = \sum_{p=0}^{N_c-1} \sigma_{cp}^2\, e^{j2\pi f_{cdp} m}\, \underline{e}_J\left(f_{csp}\right) \underline{e}_J^H\left(f_{csp}\right) \qquad m \geq 0 \tag{2-54}$$

with negative lags obtained as

$$R_{cc}(-m) = E[\,\underline{c}(n)\,\underline{c}^H(n+m)\,] = R_{cc}^H(m) \qquad m \geq 0 \tag{2-55}$$

Each matrix in the sequence is JxJ. Matrix $R_{cc}(m)$ is Hermitian only for $m = 0$; however, matrix $R_{cc}(m)$ has Toeplitz structure for all $m$ due to the spatially-induced relationship among the elements of $\underline{c}(n)$, as expressed in Equation (2-9). Equation (2-54) is analogous to Equation (2-24), and the procedure used to generate the signal covariance matrix sequence can be used to generate the clutter covariance matrix sequence.

## 2.6 Channel Output True Covariance Model

The channel output vector sequence $\{\underline{x}(n)\}$ is modeled as the sum of the signal (moving target), broadband interference (jamming), ground clutter, and receiver array noise (Equation (2-3)). These four components are assumed to be pairwise statistically independent. Thus, the channel output true covariance matrix sequence is obtained as

$$R_{xx}(m) = E[\,\underline{x}(n)\,\underline{x}^H(n-m)\,] = R_{ss}(m) + R_{ii}(m) + R_{cc}(m) + R_{ww}(m) \qquad m \geq 0 \tag{2-56}$$

with negative lags obtained as

$$(2\text{-}57) \qquad R_{xx}(-m) = E[\,\underline{x}(n)\,\underline{x}^H(n+m)\,] = R_{xx}^H(m) \qquad m \geq 0$$

Matrix $R_{xx}(m)$ is Toeplitz for all values of $m$ because each individual matrix on the right-hand-side of Equation (2-56) is Toeplitz or zero for all $m \geq 0$. Likewise, matrix $R_{xx}(0)$ is Hermitian because each individual matrix on the right-hand-side of Equation (2-56) is Hermitian for $m = 0$.

## 2.7 Signal (Moving Target) Data Generation

Moving targets are modeled as defined in Equations (2-15)-(2-21) of Section 2.1.2. That is, as the output vector sequence of a linear, stationary, discrete-time, complex-valued system in state-space form driven by a complex-valued, zero-mean, Gaussian-distributed white noise vector sequence, $\{\underline{u}(n)\}$, with diagonal covariance matrix $Q$. The initial condition for Equation (2-15a), $\underline{y}(0)$, is a complex-valued, zero-mean, Gaussian-distributed $G_s$-dimensional vector. This model is a set of $G_s$ scalar systems in parallel, and each scalar system represents a moving target. Data generation is accomplished by driving the system (2-15a) with a pseudo-random initial condition, and a pseudo-random input sequence of $N$-point duration. The initial condition is a random sample from a Gaussian distribution with mean vector zero and covariance matrix $P$. Matrix $P$ is the steady-state covariance matrix of the state vector, and it satisfies a Lyapunov equation of the form

$$(2\text{-}58) \qquad P = FPF^H + Q$$

For an asymptotically-stable system, Equation (2-58) has a positive-definite solution. Furthermore, since matrices $F$ and $Q$

are both diagonal, Equation (2-58) reduces to the following set of scalar equations,

$$P(k,k) = |F|^2 P + Q(k,k) \qquad k = 1, 2, \ldots, G_s \tag{2-59}$$

which is an equivalent expression for Equation (2-19b). Selection of $P$ as the covariance matrix of the state vector initial condition places the system model in stochastic steady-state at time $n = 0$, and it remains in stochastic steady-state. The $k$th moving target contributes $\sigma_{sk}^2$ power to each channel output, and the total signal power in each channel is

$$\sigma_s^2 = \text{diag}(P) = \sum_{k=1}^{G_s} \sigma_{sk}^2 \tag{2-60}$$

with $P(k,k) = \sigma_{sk}^2$, as defined in Equation (2-21).

Swerling Cases 1 and 2 can be generated by appropriate choice of the model parameters in model (2-16)-(2-18). For notational simplicity, consider the case of a single target, $k = 1$. For Swerling Case 1, let $a_1 = 1$ and $f_{td1} = 0$, which forces the driving noise covariance to be equal to zero, and the state-space model becomes

Swerling Case 1:

$$y(n+1) = y(n) \qquad 0 \le n \le N-1 \tag{2-61a}$$

$$\underline{s}(n) = \underline{e}_J(f_{ts1})\, y(n) \qquad 0 \le n \le N-1 \tag{2-61b}$$

$$y(0) \sim \mathcal{N}(\underline{0}, 0.5\, \sigma_{s1}^2\, I_2) \tag{2-61c}$$

where $\mathcal{N}(\underline{0}, 0.5\,\sigma_{s1}^2\,I_2)$ denotes the 2-D circular Gaussian distribution for a complex-valued scalar with mean zero and diagonal covariance (the scalar, complex-valued initial condition has variance $\sigma_{s1}^2$). For Swerling Case 2, let $a_1 = 0$, which forces the driving noise covariance to be equal to unity, and the state-space model becomes

Swerling Case 2:

(2-62a) $y(n+1) = u(n)$ $\qquad 0 \le n \le N-1$

(2-62b) $\underline{s}(n) = \underline{e}_J(f_{ts1})\, y(n)$ $\qquad 0 \le n \le N-1$

(2-62c) $u(n) \sim \mathcal{N}(\underline{0}, 0.5\, I_2)$ $\qquad 0 \le n \le N-1$

(2-62d) $y(0) \sim \mathcal{N}(\underline{0}, 0.5\,\sigma_{s1}^2\, I_2)$

Swerling Cases 3 and 4 can be modeled with the equations for Cases 1 and 2, respectively, if the initial condition vector and the input noise vector are distributed as chi-square with four degrees-of-freedom instead of Gaussian.

A note of caution is appropriate. Swerling Case 1 (also Case 3) conditions correspond to a system model which is conditionally stable, as opposed to asymptotically stable. This violates one of the conditions for applicability of the identification algorithms used in this program (as well as many other identification algorithms), and can lead to difficulties. Specifically, it has been observed in various simulations that setting $a_k = 1$ leads to canonical correlations greater than unity, which is an invalid condition. The exact theoretical answer for such cases is unity canonical correlations, but numerical issues often force the invalid result.

## 2.8 Broadband Interference (Jamming) Data Generation

Broadband interference (jamming) is modeled as defined in Section 2.1.3. That is, the broadband interference sequence, $\{\underline{i}(n)\}$, is a complex-valued, Gaussian-distributed, zero-mean, white sequence, which represents the received interference from all direct, barrage, point-souce jammers. In this model each channel receives the same amount of power from each jammer. It follows that the jamming sequence model is

$$\underline{i}(n) = \sum_{k=1}^{G_i} i_k(n)\, \underline{e}_J(f_{isk}) \qquad 0 \le n \le N-1 \tag{2-63a}$$

$$i_k(n) \sim \mathcal{N}(\underline{0}, 0.5\sigma_{ik}^2 I_2) \qquad 1 \le k \le G_i;\ 0 \le n \le N-1 \tag{2-63b}$$

where $i_k(n)$ is the $k$th jamming source white sequence with corresponding spatial frequency $f_{isk}$, and $\sigma_{ik}^2$ is the variance (power) of the $k$th jamming source at each channel output. Data generation is accomplished by generating $G_i$ complex-valued, pseudo-random, scalar, white sequences $\{i_k(n)\}$ according to Equation (2-63b), and combining them according to Equation (2-63a). The total jammer power in each channel, denoted as $\sigma_i^2$, is given as

$$\sigma_i^2 = \sum_{k=1}^{G_i} \sigma_{ik}^2 \tag{2-64}$$

for $G_i$ independent interference sources.

## 2.9 Receiver Array Noise Data Generation

Receiver array noise is modeled as described in Section 2.1.4. That is, the receiver array noise sequence, $\{\underline{w}(n)\}$, is a complex-valued, Gaussian-distributed, zero-mean, white sequence

uncorrelated from channel to channel (with diagonal covariance at each time instant),

$$(2\text{-}65a) \qquad E\left[\underline{w}(n)\underline{w}^H(n-m)\right] = \sigma_n^2 \delta_{n-m} I_J$$

$$(2\text{-}65b) \qquad \underline{w}(n) \sim \mathcal{N}(\underline{0}, 0.5\,\sigma_n^2 I_{2J}) \qquad 0 \le n \le N-1$$

where $\sigma_n^2$ is the noise power in each channel. Data generation is accomplished by generating a J-dimensional, complex-valued, pseudo-random, white vector sequence according to Equation (2-65).

## 2.10 Ground Clutter Data Generation

Ground clutter is modeled as described in Section 2.1.5. That is, the ground clutter sequence, $\{\underline{c}(n)\}$, is the sum of the return from $N_c$ ground patches in the clutter ring illuminated by the array main beam. Each patch is represented by a single complex-valued, Gaussian-distributed, zero-mean random scatterer, as indicated in Equation (2-48b), and the scatterers are assumed to be pairwise statistically-independent. Equation (2-48b) is repeated next as Equation (2-66), for convenience,

$$(2\text{-}66) \qquad \underline{c}(n) = \sum_{p=0}^{N_c-1} \eta_p\, e^{j2\pi f_{cdp} n}\, \underline{e}_J\left(f_{csp}\right) \qquad n = 0, 1, \ldots, N-1$$

$$(2\text{-}67) \qquad \eta_p \sim \mathcal{N}(\underline{0}, 0.5\,\sigma_{cp}^2\, I_2) \qquad p = 0, 1, \ldots, N_c - 1$$

As before, $\eta_p$ denotes the clutter return from the single scatterer representing the pth patch, and $f_{cdp}$ and $f_{csp}$ denote the normalized Doppler frequency and spatial frequency, respectively, of the pth clutter patch. These frequencies are computed as in Equations (2-49)-(2-50). The clutter process $\{\underline{c}(n)\}$ has true covariance matrix sequence $\{R_{cc}(m)\}$ defined as in Equations (2-54) and (2-55). Data

generation is accomplished by generating $N_c$ complex-valued, pseudo-random, scalar, random variables $\{\eta_p\}$ according to Equation (2-67), and combining them according to Equation (2-66). This procedure is computationally intensive when the number of ground patches ($N_c$) is large and the number of receive array elements (J) is large. The pth scatterer contributes $\sigma_{cp}^2$ power to each channel output, and the total ground clutter power in each channel is

$$\sigma_c^2 = \sum_{p=1}^{N_c} \sigma_{cp}^2 \qquad (2\text{-}68)$$

Equation (2-68) follows from Equations (2-48a) and (2-52).

## 2.11 Channel Output Data Generation

The channel output vector sequence $\{\underline{x}(n)\}$ is modeled as the sum of the signal (moving target), broadband interference (jamming), ground clutter, and receiver array noise. These four components are assumed to be pairwise statistically independent. Thus, the channel output vector sequence $\{\underline{x}(n)\}$ is generated as the sum of the four independent components,

$$\underline{x}(n) = \underline{s}(n) + \underline{i}(n) + \underline{c}(n) + \underline{w}(n) \qquad 0 \le n \le N-1 \qquad (2\text{-}69)$$

and the total power in each channel output is

$$\sigma_x^2 = \sigma_s^2 + \sigma_i^2 + \sigma_c^2 + \sigma_n^2 \qquad (2\text{-}70)$$

Single-channel power ratios (such as signal-to-noise ratio) can be calculated given the channel output power level for each individual component (signal; interference; clutter).

## 2.12 Covariance, Spectrum, and Graphical Issues

Diagnostics constitute a key part of the software model developed in this program. Generation of the 2-D power spectrum of the surveillance radar space/time process and plots of the spectrum and associated auto-covariance sequence provide insight into the structure and characteristics of the "true" process and the simulated data. Power spectrum and auto-covariance matrix estimates are important also. Those issues are discussed in this section.

The channel output vector sequence $\{\underline{x}(n)\}$ can be viewed as a scalar 2-D sequence due to the relationship that exists between elements of the vector processes $\underline{s}(n)$, $\underline{c}(n)$, and $\underline{i}(n)$, and because the spatially-uncorrelated white noise vector $\underline{w}(n)$ can be viewed also as a scalar 2-D white sequence. Specifically,

$$x_{k+1}(n) = x_1(n+k\tau) = x_1(n,k) \qquad 0 \le n \le N-1;\ 0 \le k \le J-1 \tag{2-71}$$

The scalar 2-D process $\{x_1(n,k)\}$ has a scalar 2-D power spectrum denoted as $\{S_{xx}(f_d,f_s)\}$, and a scalar 2-D auto-covariance sequence (ACS) denoted as $\{r_{xx}(m,\ell)\}$, where $(m,\ell)$ denotes the lag pair corresponding to the frequency pair $(f_d,f_s)$. The 2-D power spectrum and the ACS form a Fourier transform pair (see, for example, Dudgeon and Mersereau, 1984),

$$S_{xx}(f_d,f_s) = \mathcal{F}\left[r_{xx}(m,\ell)\right] = \sum_{m=-\infty}^{\infty} \sum_{\ell=-\infty}^{\infty} r_{xx}(m,\ell)\, \exp\left[-j2\pi(f_d m + f_s \ell)\right] \tag{2-72}$$

$$-0.5 \le f_d \le 0.5 \qquad \text{and} \qquad -0.5 \le f_s \le 0.5$$

$$(2\text{-}73) \qquad r_{xx}(m,\ell) = \mathcal{F}^{-1}[S_{xx}(f_d,f_s)] = \int_{-0.5}^{0.5}\int_{-0.5}^{0.5} S_{xx}(f_d,f_s)\,\exp[j2\pi(f_d m + f_s \ell)]\,df_d\,df_s$$

$$-\infty \le m \le \infty \qquad \text{and} \qquad -\infty \le \ell \le \infty$$

In this transform pair the ACS is infinite and the power spectrum is continuous. Neither of these two conditions is true in practical applications such as surveillance radar. In fact, the number of lags available is determined by the number of channels and the number of pulses in one CPI, and the spectrum is sampled at sampling intervals determined also by the number of channels and the number of pulses in one CPI. For these conditions the relation that applies is the DFT and its inverse; namely,

$$(2\text{-}74a) \qquad S_{xx}(f_d,f_s) = F[r_{xx}(m,\ell)] = \sum_{m=-N+1}^{N-1}\sum_{\ell=-J+1}^{J-1} r_{xx}(m,\ell)\,\exp[-j2\pi(f_d m + f_s \ell)]$$

$$(2\text{-}74b) \qquad f_d = k_d \Delta f_d \qquad -N+1 \le k_d \le N-1$$

$$(2\text{-}74c) \qquad f_s = k_s \Delta f_s \qquad -J+1 \le k_s \le J-1$$

$$(2\text{-}74d) \qquad \Delta f_d = \frac{1}{2N-1}$$

$$(2\text{-}74e) \qquad \Delta f_s = \frac{1}{2J-1}$$

$$(2\text{-}75a) \qquad r_{xx}(m,\ell) = \mathbf{F}^{-1}[S_{xx}(f_d,f_s)] \qquad -N+1 \le m \le N-1;\ -J+1 \le \ell \le J-1$$

$$(2\text{-}75b) \qquad r_{xx}(m,\ell) = \sum_{f_s=-0.5}^{0.5}\sum_{f_d=-0.5}^{0.5} S_{xx}(f_d,f_s)\,\exp[j2\pi(f_d m + f_s \ell)]\,\Delta f_d\,\Delta f_s$$

$$(2\text{-}75c) \qquad r_{xx}(m,\ell) = \frac{1}{(2J-1)(2N-1)} \sum_{f_s=-0.5}^{0.5} \sum_{f_d=-0.5}^{0.5} S_{xx}(f_d,f_s)\, \exp[j2\pi(f_d m + f_s \ell)]$$

Parameters $\Delta f_d$ and $\Delta f_s$ determine the spectrum's frequency resolution along the Doppler and spatial axes, respectively. Periodic sampling of the continuous spectrum causes the ACS to be repeated periodically in the lag domain. Likewise, the sampled spectrum is repeated periodically in the frequency domain because the ACS is available only at discrete times.

It is possible to express the 2-D ACS in terms of the 2-D sequence $\{x_1(n,k)\}$ as follows:

$$(2\text{-}76) \qquad r_{xx}(m,\ell) = E[x_1(n,k)\, x_1^*(n-m,k-\ell)] \qquad m \geq 0;\ \ell \geq 0$$

with negative lag values determined according to

$$(2\text{-}77) \qquad r_{xx}(-m,\ell) = r_{xx}^*(m,-\ell) \qquad m \geq 0;\ \ell \geq 0$$

$$(2\text{-}78) \qquad r_{xx}(m,-\ell) = r_{xx}^*(-m,\ell) \qquad m \geq 0;\ \ell \geq 0$$

$$(2\text{-}79) \qquad r_{xx}(-m,-\ell) = r_{xx}^*(m,\ell) \qquad m \geq 0;\ \ell \geq 0$$

The channel output true covariance matrix sequence, $\{R_{xx}(m)\}$, can be expressed also in terms of the channel output 2-D ACS using Equations (2-76)-(2-79). The JxJ covariance matrix sequence for the process $\{\underline{x}(n)\}$ is defined in Equations (2-54) and (2-55). For each $m$, matrix $R_{xx}(m)$ can be expressed in terms of the elements of the 2-D ACS as

$$(2\text{-}80)\qquad R_{xx}(m)=\begin{bmatrix} r_{xx}(m,0) & r_{xx}(m,-1) & \cdots & r_{xx}(m,-J+2) & r_{xx}(m,-J+1) \\ r_{xx}(m,1) & r_{xx}(m,0) & \cdots & r_{xx}(m,-J+3) & r_{xx}(m,-J+2) \\ \vdots & \vdots & \ddots & \vdots & \vdots \\ r_{xx}(m,J-2) & r_{xx}(m,J-3) & \cdots & r_{xx}(m,0) & r_{xx}(m,-1) \\ r_{xx}(m,J-1) & r_{xx}(m,J-2) & \cdots & r_{xx}(m,1) & r_{xx}(m,0) \end{bmatrix}$$

Notice that $R_{xx}(m)$ is defined completely by the first row and the first column, as befits its Toeplitz structure. Based on Equations (2-77)-(2-79), $R_{xx}(m)$ is Hermitian only for $m = 0$, as stated previously.

Equation (2-74a) can be expressed as a matrix equation of the form

$$(2\text{-}81)\qquad S_{xx} = T_L\, R_{xx}\, T_R$$

where $S_{xx}$ is the (2J-1)x(2N-1) power spectrum matrix, $T_L$ is the (2J-1)x(2J-1) DFT matrix, $T_R$ is the (2N-1)x(2N-1) DFT matrix, and $R_{xx}$ is the (2J-1)x(2N-1) ACS matrix defined as

$$(2\text{-}82)\qquad R_{xx}=\left[\begin{array}{ccc:ccc} r_{xx}(-N+1,-J+1) & \cdots & r_{xx}(-1,-J+1) & r_{xx}(0,-J+1) & \cdots & r_{xx}(N-1,-J+1) \\ \vdots & \ddots & \vdots & \vdots & \ddots & \vdots \\ r_{xx}(-N+1,-1) & \cdots & r_{xx}(-1,-1) & r_{xx}(0,-1) & \cdots & r_{xx}(N-1,-1) \\ \hdashline r_{xx}(-N+1,0) & \cdots & r_{xx}(-1,0) & r_{xx}(0,0) & \cdots & r_{xx}(N-1,0) \\ \vdots & \ddots & \vdots & \vdots & \ddots & \vdots \\ r_{xx}(-N+1,J-1) & \cdots & r_{xx}(-1,J-1) & r_{xx}(0,J-1) & \cdots & r_{xx}(N-1,J-1) \end{array}\right]$$

DFT matrices $T_L$ and $T_R$ operate on the columns and rows, respectively, of the ACS matrix $R_{xx}$ to implement the 2-D DFT. It is assumed herein that the DFT matrices also include any row and/or column shift operations necessary to generate a spectrum matrix with origin at the (J,N)th element. Additionally, it may be necessary to take the absolute value of the right-hand-side

Equation (2-81) in order to obtain the true real-valued spectrum; this is a function of the way a specific DFT is implemented. The partitions on $R_{xx}$ in Equation (2-82) represent the four quadrants, Q1 through Q4, of the 2-D plane, with the lower-right partition corresponding to Q1; specifically,

$$R_{xx} \Leftrightarrow \left[\begin{array}{c|c} Q2 & Q4 \\ \hline Q3 & Q1 \end{array}\right] \tag{2-83}$$

Notice that the origin is assigned to Q1. This agrees with the convention adopted in most three-dimensional (3-D) software graphics packages, including MATLAB. The quadrants are shown in Figure 2-3, where the axes are drawn in agreement with MATLAB's 3-D graphics default axes orientation and viewing angles.

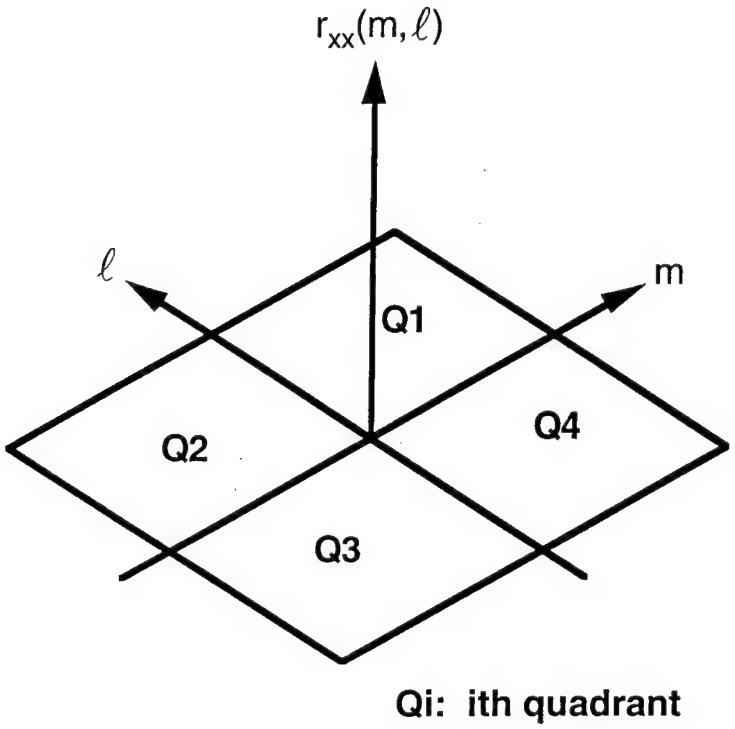


*Figure 2-3. MATLAB two-dimensional grid definition for default view angles (azimuth and elevation).*

In the approach formulated herein for the channel output true covariance model, the covariance matrix sequence is generated directly, without having to generate the power spectrum. This is appropriate for generating the inputs required by identification and detection routines when running "known covariance" cases. However, it is difficult to appreciate the features of the channel output by examination of either the true ACS or the true covariance matrix sequence. In contrast, visual examination of a 3-D plot of the power spectrum is very informative.

Given a true ACS or covariance matrix sequence, the (2J-1)x(2N-1) power spectrum matrix $S_{xx}$ is obtained via Equation (2-81), and a 3-D plot can be generated at frequency resolutions determined by Equations (2-74d) and (2-74e). The resulting plot will exhibit the principal features present in the true covariance model, but will have three drawbacks. First, the frequency resolution specified by Equations (2-74d) and (2-74e) is the coarsest resolution possible (determined by the fixed values J and N). Second, the frequency leakage level resulting from the Fourier transformation in Equation (2-81) is the highest possible because the true ACS lags beyond those specified in Equation (2-75) are unavailable, which is equivalent to multiplying the infinite-duration true ACS by a rectangular lag window defined with its corners at the lag pairs: (N-1,J-1), (-N+1,J-1), (-N+1,-J+1), and (N-1,-J+1). Third, for large values of N and/or J, the numerical evaluation of Equation (2-81) is inefficient because the length of the required transforms are odd numbers (2N-1 and 2J-1), and efficient DFT algorithms are unavailable, in general, for large and odd length values.

Each of the drawbacks mentioned above can be addressed, as shown next. The first drawback is overcome by "padding" the true ACS with zeros. The second drawback is mitigated by applying a

low-sidelobe lag window to the finite-duration true ACS. Use of a lag window improves frequency leakage but introduces a loss in frequency resolution (with the result that features extend over a larger frequency band). Finally, the third drawback is eliminated by forcing the length of the zero-padded ACS along each axis to be an even integer that is a power of two, which allows use of Fast Fourier Transform (FFT) algorithms. To express these steps mathematically, first define an $N_f x N_f$ zero-padded and windowed ACS matrix $\tilde{R}_{xx}$ as

$$\tilde{R}_{xx} = \begin{bmatrix} W \otimes R_{xx} & [0] \\ [0] & [0] \end{bmatrix} \tag{2-84}$$

where $W$ is a (2J-1)x(2N-1) lag window matrix and $\otimes$ denotes the Schur product, as before. The null sub-matrices in Equation (2-84), denoted as [0], represent appropriately-dimensioned matrices of zeros. The integer $N_f$ is selected to be a power of two such that $N_f > \max(2J-1, 2N-1)$. Then define an $N_f x N_f$ high-resolution power spectrum matrix $\tilde{S}_{xx}$ as

$$\tilde{S}_{xx} = \left| T_L \tilde{R}_{xx} T_R \right| \tag{2-85}$$

DFT matrices $T_L$ and $T_R$ in Equation (2-72) are both $N_f x N_f$, and as before, include any row and/or column shift operations necessary to generate a spectrum matrix with origin at the $(N_f/2, N_f/2)$th element. The absolute value operation in Equation (2-85) insures that the spectrum is real-valued, and is necessary in this case because the enhanced ACS matrix, $\tilde{R}_{xx}$, lacks symmetry with respect to its middle element, which generates complex-valued terms in the product $T_L \tilde{R}_{xx} T_R$ (this effect is common to most DFT implementations, and taking the absolute value generates the desired result). The frequency resolution associated with spectrum $\tilde{S}_{xx}$ is

$$\Delta f_d = \Delta f_s = \Delta f = \frac{1}{N_f} \tag{2-86}$$

Finally, the lag window matrix W is selected as the (2J-1)x(2N-1) matrix formed from a real-valued, finite-duration, separable, 2-D lag window sequence $\{\omega(m,\ell)\}$; that is,

$$\omega(m,\ell) = \omega_1(m)\,\omega_1(\ell) \qquad -N+1 \le m \le N-1;\ -J+1 \le \ell \le J-1 \tag{2-87}$$

$$W = \left[\begin{array}{ccc|ccc} \omega(-N+1,-J+1) & \cdots & \omega(-1,-J+1) & \omega(0,-J+1) & \cdots & \omega(N-1,-J+1) \\ \vdots & \ddots & \vdots & \vdots & \ddots & \vdots \\ \omega(-N+1,-1) & \cdots & \omega(-1,-1) & \omega(0,-1) & \cdots & \omega(N-1,-1) \\ \hline \omega(-N+1,0) & \cdots & \omega(-1,0) & \omega(0,0) & \cdots & \omega(N-1,0) \\ \vdots & \ddots & \vdots & \vdots & \ddots & \vdots \\ \omega(-N+1,J-1) & \cdots & \omega(-1,J-1) & \omega(0,J-1) & \cdots & \omega(N-1,J-1) \end{array}\right] \tag{2-88}$$

where $\{\omega_1(\bullet)\}$ is a real-valued, one-dimensional (1-D) lag window sequence. A 1-D lag window normalized to have unity value at the origin ($m = 0$) is preferred because it preserves total power. Since the 2-D window sequence is separable, the spectrum of the lag window matrix (2-88) is circularly symmetric.

All the relations introduced heretofore are based on true quantities, as opposed to estimated quantities, because only the true model has been considered up to this point. However, several relations involving estimates of covariance and spectra are relevant for data generation and diagnostics, and are introduced below. Prior to that it is convenient to introduce the concept of an extended 2-D sequence $\{\tilde{x}_1(n,k)\}$ obtained by padding the sequence $\{x_1(n,k) \mid n = 0, 1, \ldots, N-1; k = 0, 1, \ldots, J-1\}$ with zeros as

$$\tilde{x}_1(n,k) = \begin{cases} x_1(n,k) & 0 \le n \le N-1;\ \ 0 \le k \le J-1 \\ 0 & N \le n \le 2N-2;\ \ J \le k \le 2J-2 \end{cases} \tag{2-89}$$

This extended sequence is important in ACS and spectrum estimator definitions established next.

Given the 2-D sequence $\{x_1(n,k)\}$, the non-circular, biased, time-average estimate of the ACS for $\{x_1(n,k)\}$ is defined as

$$\hat{r}_{xx}(m,\ell) = \frac{1}{JN} \sum_{n=m}^{N-1} \sum_{k=\ell}^{J-1} x_1(n,k)\, x_1^*(n-m,k-\ell) \qquad (2\text{-}90)$$

$$0 \le m \le N-1$$

$$0 \le \ell \le J-1$$

where the caret (^) over a variable denotes an estimator, or estimate, of the variable. A similar formula (with different limits for the summations) is available to estimate the ACS for negative lags, but it is simpler to obtain the ACS estimate for negative lags according to the equivalence relations

$$\hat{r}_{xx}(-m,\ell) = \hat{r}_{xx}^*(m,-\ell) \qquad (2\text{-}91)$$

$$0 \le m \le N-1; \quad 0 \le \ell \le J-1$$

$$\hat{r}_{xx}(m,-\ell) = \hat{r}_{xx}^*(-m,\ell) \qquad (2\text{-}92)$$

$$0 \le m \le N-1; \quad 0 \le \ell \le J-1$$

$$\hat{r}_{xx}(-m,-\ell) = \hat{r}_{xx}^*(m,\ell) \qquad (2\text{-}93)$$

$$0 \le m \le N-1; \quad 0 \le \ell \le J-1$$

Notice that Equations (2-91)-(2-93) are analogous to the negative lag equations for the true ACS, Equations (2-77)-(2-79).

Alternative ACS estimators are obtained via modifications to Equation (2-90). An unbiased, non-circular estimator is obtained by replacing the factor JN in the denominator of Equation (2-90) by the factor $(J-\ell)(N-m)$. In the limit as both $J \to \infty$ and $N \to \infty$, the estimation error approaches zero in an unbiased estimate, but approaches a fixed, non-zero value in a biased estimate. A non-circular, unbiased, time-average ACS estimate is transformed into

a biased ACS estimate by appropriately scaling the unbiased estimate as

$$\hat{r}_{xxb}(m,\ell) = \omega_t(m,\ell)\,\hat{r}_{xxu}(m,\ell) \qquad -N+1 \le m \le N-1;\ -J+1 \le \ell \le J-1 \tag{2-94}$$

where the u and b subscripts denote unbiased and biased estimates, respectively, since both types of estimates appear in the same equation. In subsequent usage, however, the estimator type subscript is dropped when the type of estimate (or estimator) used is clear from the context and confusion is unlikely to occur. The 2-D sequence $\{\omega_t(m,\ell)\}$ is a real-valued, separable, lag window sequence computed as the product of two normalized 1-D triangular sequences,

$$\omega_t(m,\ell) = \omega_{td}(m)\,\omega_{ts}(\ell) \qquad -N+1 \le m \le N-1;\ -J+1 \le \ell \le J-1 \tag{2-95}$$

$$\omega_{td}(m) = \frac{1}{N}\{1, 2, \ldots, N\text{-}1, N, N\text{-}1, \ldots, 2, 1\} \tag{2-96}$$

$$\omega_{ts}(\ell) = \frac{1}{J}\{1, 2, \ldots, J\text{-}1, J, J\text{-}1, \ldots, 2, 1\} \tag{2-97}$$

Notice that the central element (corresponding to $m = \ell = 0$) of all three sequences is unity. As a consequence, the variance (total power) is unchanged after the scaling by $\{\omega_t(m,\ell)\}$. A (2J-1)x(2N-1) lag window matrix $W_t$ is associated with the 2-D sequence $\{\omega_t(m,\ell)\}$, as in Equations (2-87) and (2-88).

An <u>unbiased, circular</u> estimator is obtained by repeating the finite sequence over the time and space domain, which results in that for an (N, J)-point sequence all lags are computed as the sum of JN non-zero products. Of more relevance to the approach pursued herein, Estimator (2-90) is equivalent to a <u>circular, biased, time-average estimate of the ACS</u> for $\{\tilde{x}_1(n,k)\}$ computed as

$$\hat{r}_{xx}(m,\ell) = \frac{1}{JN} \sum_{n=m}^{2N-2} \sum_{k=\ell}^{2J-2} \tilde{x}_1(n,k)\, \tilde{x}_1^*(n-m,k-\ell) \qquad \begin{matrix} 0 \le m \le N-1 \\ 0 \le \ell \le J-1 \end{matrix} \tag{2-98}$$

with negative lags computed as in Equations (2-91)-(2-93). Even though it is calculated as a circular estimator, estimator (2-98) is equivalent to estimator (2-90) because the extended sequence can be repeated over the time and space domain without altering the sum of products, in relation to Equation (2-90), due to the zeros present in the extended sequence.

Other ACS estimators can be defined, and each one has distinct properties. For model identification estimator (2-90) is preferred because it leads to improved model parameter estimates. In summary, for a 2-D sequence of duration (N, J), an ACS estimate of maximum duration (2N-1, 2J-1) is obtained.

The 2-D periodogram, denoted as $\hat{S}_{xx}(f_d,f_s)$, is an estimator of the power spectrum of $\{x_1(n,k)\}$, that is obtained as the 2-D DFT of the non-circular, unbiased, time-average ACS estimate (see, for example, Oppenheim and Schafer, 1975),

$$\hat{S}_{xx}(f_d,f_s) = F\left[\hat{r}_{xx}(m,\ell)\right] = \sum_{m=-N+1}^{N-1} \sum_{\ell=-J+1}^{J-1} \hat{r}_{xx}(m,\ell) \exp\left[-j2\pi(f_d m + f_s \ell)\right] \tag{2-99a}$$

$$f_d = k_d \Delta f_d \qquad -N+1 \le k_d \le N-1 \tag{2-99b}$$

$$f_s = k_s \Delta f_s \qquad -J+1 \le k_s \le J-1 \tag{2-99c}$$

$$\Delta f_d = \frac{1}{2N-1} \tag{2-99d}$$

(2-99e) $$\Delta f_s = \frac{1}{2J-1}$$

It follows that the inverse transform relation is

(2-100a) $$\hat{r}_{xx}(m,\ell) = \mathbf{F}^{-1}\left[\hat{S}_{xx}(f_d,f_s)\right] \qquad -N+1 \le m \le N-1;\ -J+1 \le \ell \le J-1$$

(2-100b) $$\hat{r}_{xx}(m,\ell) = \sum_{f_s=-0.5}^{0.5} \sum_{f_d=-0.5}^{0.5} \hat{S}_{xx}(f_d,f_s)\, \exp\left[j2\pi(f_d m + f_s \ell)\right]\, \Delta f_d\, \Delta f_s$$

(2-100c) $$\hat{r}_{xx}(m,\ell) = \frac{1}{(2J-1)(2N-1)} \sum_{f_s=-0.5}^{0.5} \sum_{f_d=-0.5}^{0.5} \hat{S}_{xx}(f_d,f_s)\, \exp\left[j2\pi(f_d m + f_s \ell)\right]$$

Notice that transform equation pair (2-99) and (2-100) for the estimators is analogous to transform equation pair (2-74) and (2-75), which is valid for the true functions.

In most texts the periodogram is defined first as a function of the data sequence, and then the equivalence with Equation (2-99) is stated. Specifically, the periodogram is computed directly using from the extended 2-D sequence as (see, for example, Oppenheim and Schafer, 1975)

(2-101a) $$\hat{S}_{xx}(f_d,f_s) = \frac{1}{(2J-1)(2N-1)} \left|\mathbf{F}\left[\tilde{x}_1(n,k)\right]\right|^2$$

(2-101b) $$\hat{S}_{xx}(f_d,f_s) = \frac{1}{(2J-1)(2N-1)} \left| \sum_{n=0}^{2N-2} \sum_{k=0}^{2J-2} \tilde{x}_1(n,k)\, \exp\left[-j2\pi(f_d n + f_s k)\right] \right|^2$$

(2-101c) $$f_d = k_d \Delta f_d \qquad -N+1 \le k_d \le N-1$$

(2-101d) $$f_s = k_s \Delta f_s \qquad -J+1 \le k_s \le J-1$$

(2-101e) $$\Delta f_d = \frac{1}{2N-1}$$

(2-101f) $$\Delta f_s = \frac{1}{2J-1}$$

The frequency-domain pair and resolution parameters are repeated in this equation in order to emphasize the equivalence with Equation (2-99). In the frequency domain, total power (variance) is estimated according to the relation

(2-102)

$$\hat{r}_{xx}(0,0) = \sum_{f_s=-0.5}^{0.5} \sum_{f_d=-0.5}^{0.5} \hat{S}_{xx}(f_d,f_s)\, \Delta f_d\, \Delta f_s = \frac{1}{(2J-1)(2N-1)} \sum_{f_s=-0.5}^{0.5} \sum_{f_d=-0.5}^{0.5} \hat{S}_{xx}(f_d,f_s)$$

Equation (2-102) corresponds to Equation (2-100) with $m = \ell = 0$, and can be used to provide one indication of validity of a spectrum estimate.

The relations in Equations (2-89)-(2-101) can be summarized in a diamond-shaped diagram, as in Figure 2-4. This diagram is useful for visualization of the analytical issues that relate the 2-D sequences. The corners of the diamond, labeled **1** through **4**, represent the four 2-D sequences, and the sides of the diamond represent the analytical expressions that relate the sequences to each other. Notice that only two operations are reversible, **1** to **4**, and **2** to **3**. The periodogram operation (**4** to **3**) and the two ACS estimation operations (**1** to **2**; **4** to **2**) are irreversible because, since these operations are nonlinear, phase information is lost in the generation of second-order statistical information (power spectrum and ACS).

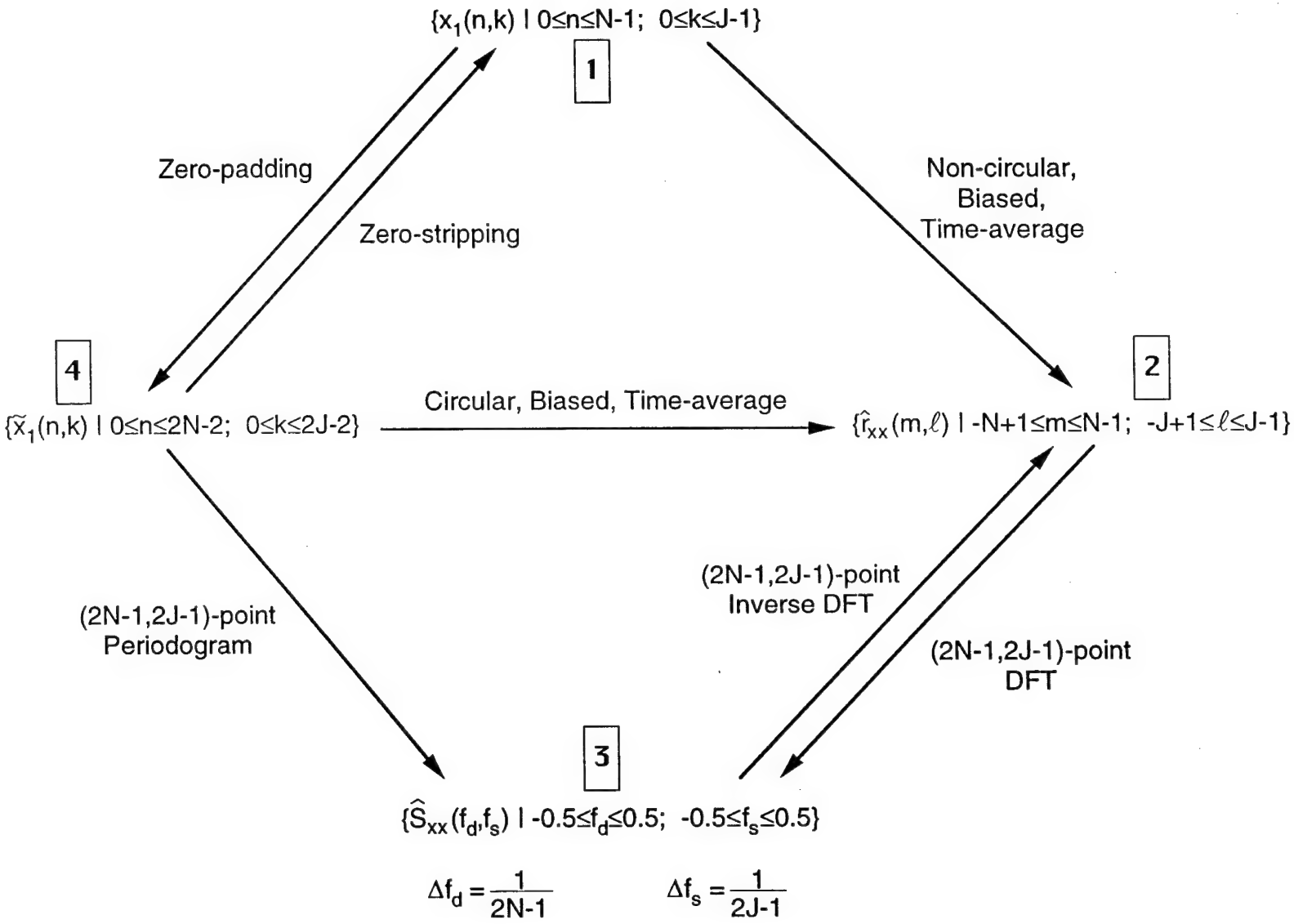


*Figure 2-4. Two-dimensional data analysis relations.*

Several modifications have been proposed to improve the basic periodogram. An important modification is the inclusion of a 2-D window in the right-hand-side of either Equation (2-99a) or Equation (2-101a). In general, the power spectrum estimate is different if a given window is applied to the ACS estimate or to the data sequence. The numerical differences, however, can be small. The relevant terminology is different also: a given window is referred to as a lag window when applied to an ACS estimate, and as a data window when applied to a data sequence. Use of a window in either context leads to a more stable power spectrum estimate (less error variance), at the expense of less resolution. When windowed data is used to generate the spectrum, the procedure is referred to as the modified periodogram method. And when the windowed ACS is used to generate the spectrum (as in Equations (2-84) and (2-85) for true functions), the procedure is referred to as the Blackman-Tukey method.

Another approach to improve the periodogram stability is applicable only to the data-based periodogram definition, Equation (2-101a). This approach consists of three steps: (a) partition the given data sequence into several shorter segments (with or without segment overlap), (b) computation of a periodogram from each data segment, and (c) averaging the resulting periodograms. A data window may be applied to the individual sequence segments (see, for example, Oppenheim and Schafer, 1975). As with the prior modification, enhanced spectral estimate stability is attained at the cost of reduced resolution.

## 3.0 SAMPLE SIMULATION RESULTS

Several runs were made to validate the analytic/software model, with emphasis on the ground clutter component because it is the most complex segment of the model. For that purpose the baseline case defined by Ward (1994) has been adopted, with the parameters as listed in Tables 3-1 and 3-2. These tables list the parameter symbol, description, and value for Ward's baseline case in the units used in SSC's MATLAB-based software. For simplicity, normalized values are used for noise, signal, and jammer powers.

Software validation of the MATLAB-based simulation included exercised it with the values listed in Tables 3-1 and 3-2 as inputs. Simulation outputs include the power ratio parameters signal-to-noise ratio (SNR), jammer-to-noise ratio (JNR), and CNR. Several plots are simulation outputs also, including CNR as a function of azimuth, and true and estimated 2-D spectra. For the baseline case in Tables 3-1 and 3-2 the power ratio parameters are: 0 dB SNR, 38.1 dB JNR, and 46.1 dB CNR. Ward's results for these same conditions are (Ward, 1994): 0 dB SNR, 38 dB JNR, and 47 dB CNR. The 0.9 dB disagreement in the CNR value is due to small differences between the two models. Ward (1994) does not list the values he uses for the physical constants, and does not provide analytical expressions for several parameters, such as receiver noise power spectral density, transmit antenna pattern, and receive column pattern beamforming gain.

Figure 3-1 presents CNR as a function of azimuth, $\xi_c(\phi,\theta_0)$, for Ward's baseline case, with $\theta_0$ calculated as in Figure 2-2. This figure corresponds to Figure 10 in (Ward, 1994), and is presented here in the same scale (for both axes) and with gridlines, for ease of comparison. Notice that the figures are very similar in outline and scale. The maximum value of $\xi_c(\phi,\theta_0)$ is 38.1 dB for $\phi = 0°$, whereas the maximum value extracted visually from Ward's Figure

10 is approximately 38.5 dB. This discrepancy is consistent with the difference in total CNR (0.9 dB) between the two simulations.

| SYMBOL | DESCRIPTION | VALUE |
|---|---|---|
| J | Number of azimuth axis array elements (or sub-arrays), which is the number of azimuth channels | 18 |
| N | Number of pulses in one CPI, which is the duration of the channel output vector sequence | 18 |
| $J_e$ | Number of elevation axis array elements beamformed into one azimuth channel | 4 |
| $P_t$ | Peak transmitted power | 200 kW |
| $T_u$ | Uncompressed pulse duration | 200 μs |
| $f_{PRF}$ | Pulse repetition frequency | 300 Hz |
| $f_C$ | Radiation frequency | 450 MHz |
| $f_B$ | Receiver instantaneous bandwidth | 4 MHz |
| $G_a(\phi,\theta_0)$ | Transmit array pattern | Uniform |
| $G_o$ | Transmit pattern gain | 22 dB |
| $G_e$ | Array element gain | 4 dB |
| $G_b$ | Array element backlobe pattern gain | -30 dB |
| $\sigma_n^2$ | Receiver noise power in each channel | 1 (normalized) |
| $F_n$ | Noise figure | 3 dB |
| $L_s$ | System losses | 4 dB |

*Table 3-1. Radar system parameters for Ward (1994) baseline case.*

| SYMBOL | DESCRIPTION | VALUE |
|---|---|---|
| $H_p$ | Platform altitude | 9 km |
| $V_p$ | Platform velocity | 50 m/s |
| $r_c$ | Range from platform to ground clutter range ring illuminated by array main beam | 130 km |
| $\gamma$ | Aircraft platform crab angle | 0 deg |
| $\phi$ | Array main beam azimuth angle | 0 deg |
| $N_c$ | Number of ground clutter patches in the range ring illuminated by array main beam | 361 |
| $G_s$ | Number of moving targets | 1 |
| a | Target model damping coefficient | 0.99 |
| $V_t$ | Target radial velocity | 33.3333 m/s |
| $\phi_t$ | Target azimuth angle | 0 deg |
| $\theta_t$ | Target elevation angle | 0 deg |
| $\sigma_s^2$ | Target power in each channel | 1 |
| $G_i$ | Number of jamming sources | 2 |
| $\phi_i$ | Jamming sources azimuth angles | 25 deg; -40 deg |
| $\theta_i$ | Jamming sources elevation angles | 0 deg; 0 deg |
| $\sigma_i^2$ | Jammer powers in each channel | 3310 dB; 3000 dB |

*Table 3-2. Scenario parameters for Ward (1994) baseline case.*

CNR as a function of azimuth is presented in Figure 3-2 for Ward's baseline case, except that the array pattern function, $G_a(\phi,\theta_0)$, is a Dolph-Chebyshev taper with 30 dB sidelobe attenuation level. For ease of comparison, the axes scale is the same as in Figure 3-1. As expected, the CNR reflects the broader main beam and lower sidelobes in relation to the conditions of Figure 3-1. The maximum value of $\xi_c(\phi,\theta_0)$ is 38.1 dB for $\phi = 0°$, and the total CNR is 51.6 dB. Both plots have the same maximum value because the array pattern function is normalized to unity at the main beam direction (the constant factor $U$ in Equation (2-43)).

A plot of the true power spectrum for Ward's baseline case is presented in Figures 3-3 and 3-4. Figure 3-3 is a 3-D plot of the logarithm (base 10) of the spectrum, and Figure 3-4 is a contour plot of the spectrum in Figure 3-3. The spectrum was normalized so that its maximum value is 0 dB. This spectrum was computed using the Blackman-Tukey method, which consists of applying the DFT to the product of the true ACS and a lag window (Equations (2-84) and (2-85)). A Dolph-Chebyshev window with 60 dB sidelobes was used to enhance the spectral features, and padding with 110 zeros along each axis was used to increase the plot resolution to $\Delta f_d = \Delta f_s = 1/128$. In both figures, notice the clutter ridge at $\alpha = 45°$ (corresponding to $\upsilon = 1$), with mainlobe at $f_d = 0$, $f_s = 0$. Other relevant parameters calculated by the program include main beam elevation angle, $\theta_0 = -4.41°$, and grazing angle, $\psi_c = 3.53°$. The spectral ridges due to the two jammers, at $f_s = 0.21$ (for $\phi_{i1} = 25°$) and $f_s = -0.32$ (for $\phi_{i2} = -40°$), stand out in both figures. However, the moving target at $f_d = 0.334$ and $f_s = 0$ is noticeable only in the contour plot, Figure 2-8, because the jammer ridge at spatial frequency $f_s = -0.32$ hides it in Figure 3-3.

The plots presented in Figures 3-3 and 3-4 are based on the true ACS generated as described in Sections 2.1.2 through 2.1.6 herein. In contrast, Figures 3-5 and 3-6 present 3-D and contour

plots, respectively, of the logarithm of the spectrum generated using the modified periodogram method applied to ten independent zero-padded (with 110 zeros) pseudo-random realizations of the channel output sequence generated as described in Sections 2.1.7 through 2.1.11. A Dolph-Chebyshev data window with 60 dB (power) sidelobes was applied to each realization prior to the computation of its periodogram. The ten periodograms were averaged to obtain the periodogram shown in these two figures. Notice the similarity of Figures 3-5 and 3-6 with Figures 3-3 and 3-4, respectively, which indicates that the data-based spectrum based on only ten realizations is very close to the true ACS-based spectrum.

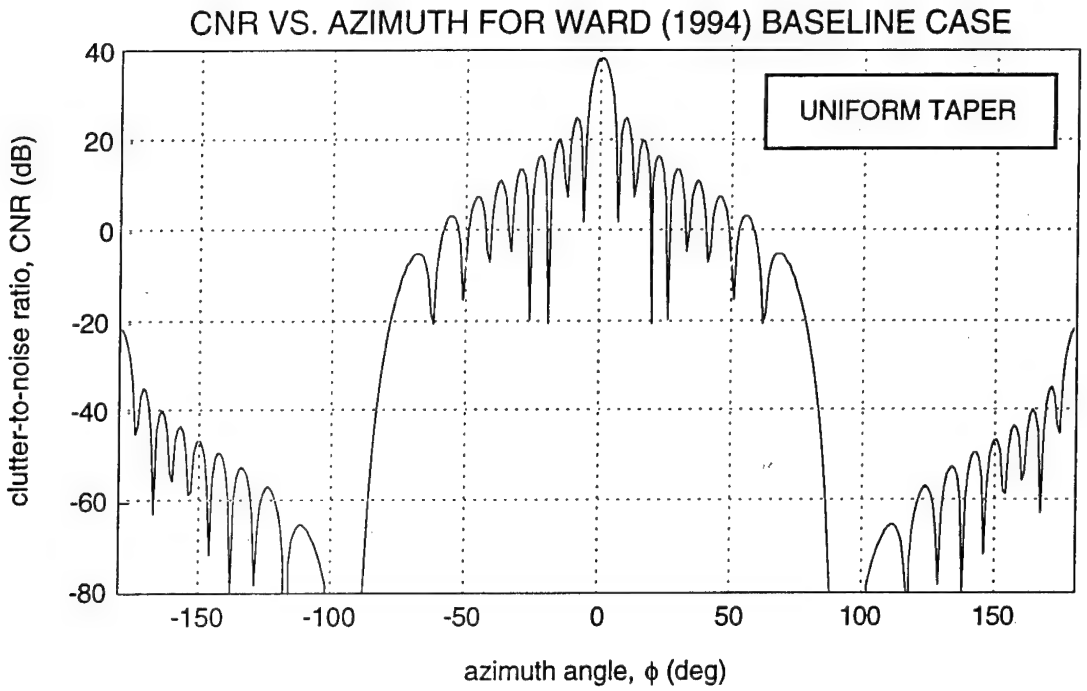


*Figure 3-1. CNR vs. azimuth angle for Ward's baseline case.*

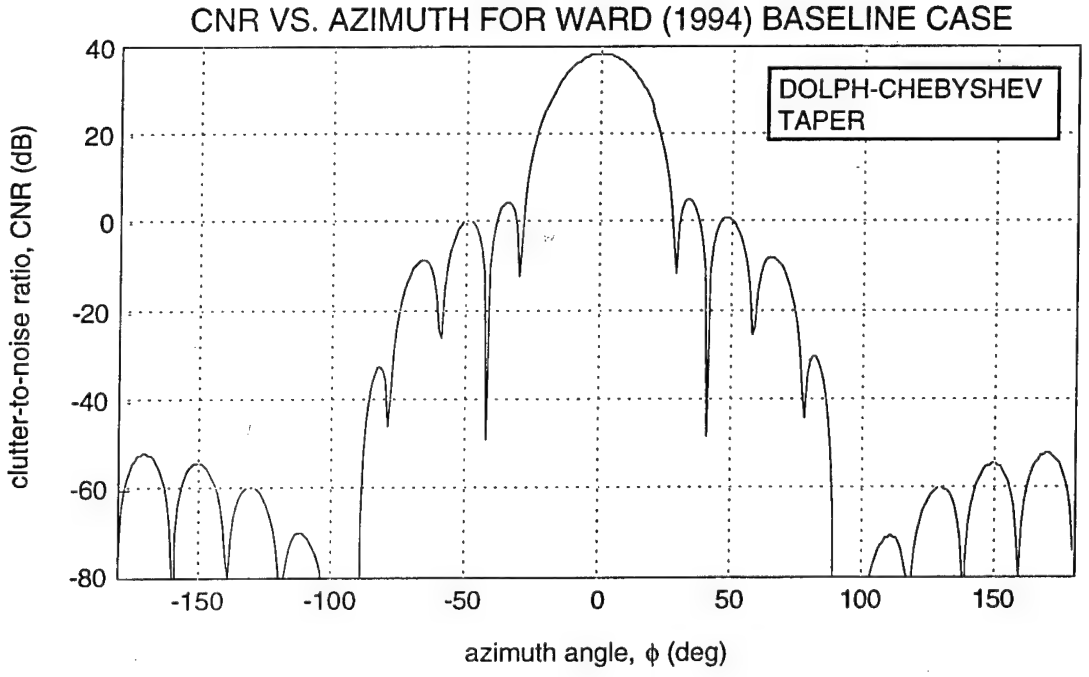


*Figure 3-2. CNR vs. azimuth angle for Ward's baseline case with Dolph-Chebyshev transmit array taper.*

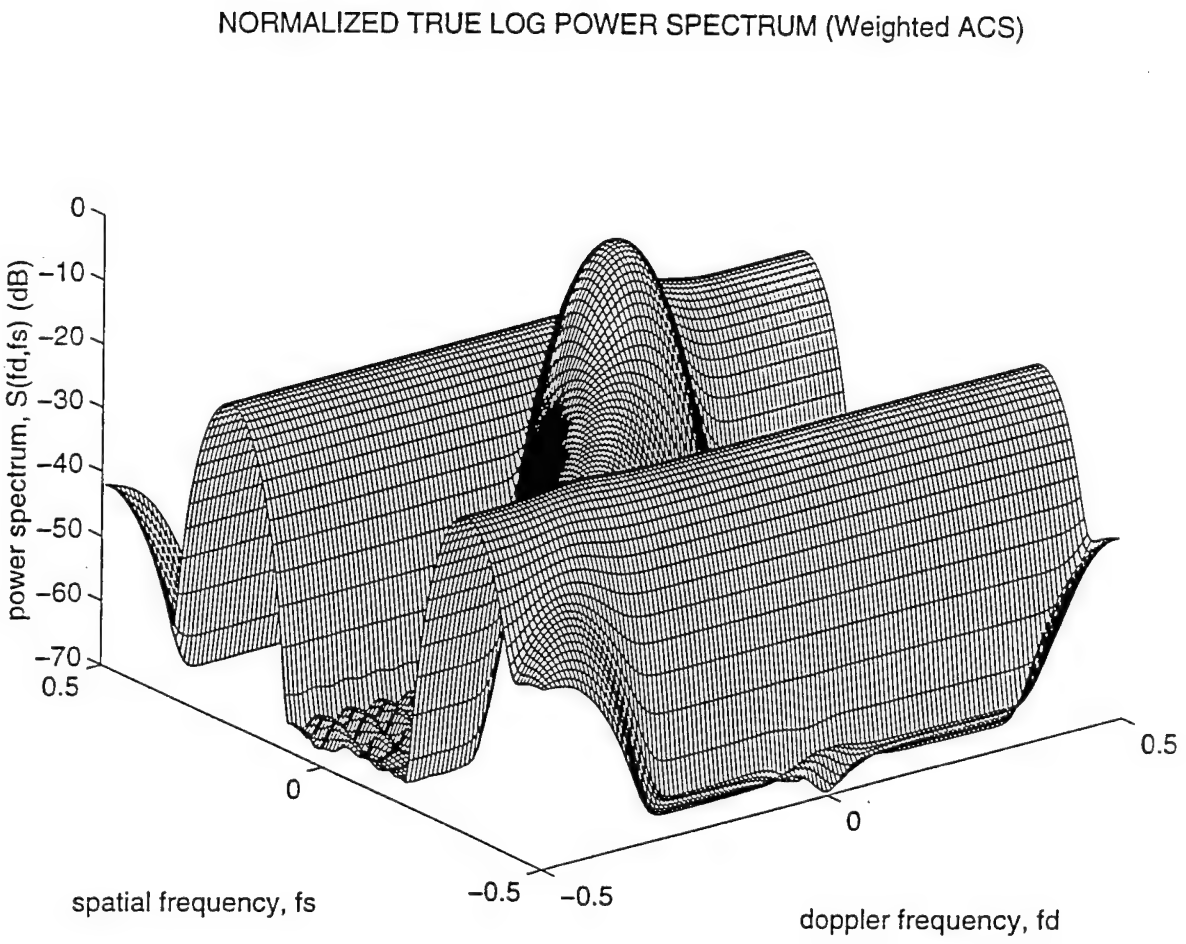


*Figure 3-3. Logarithm of the normalized true power spectrum of the array output for Ward's baseline case (DFT of the Dolph-Chebyshev weighted ACS).*

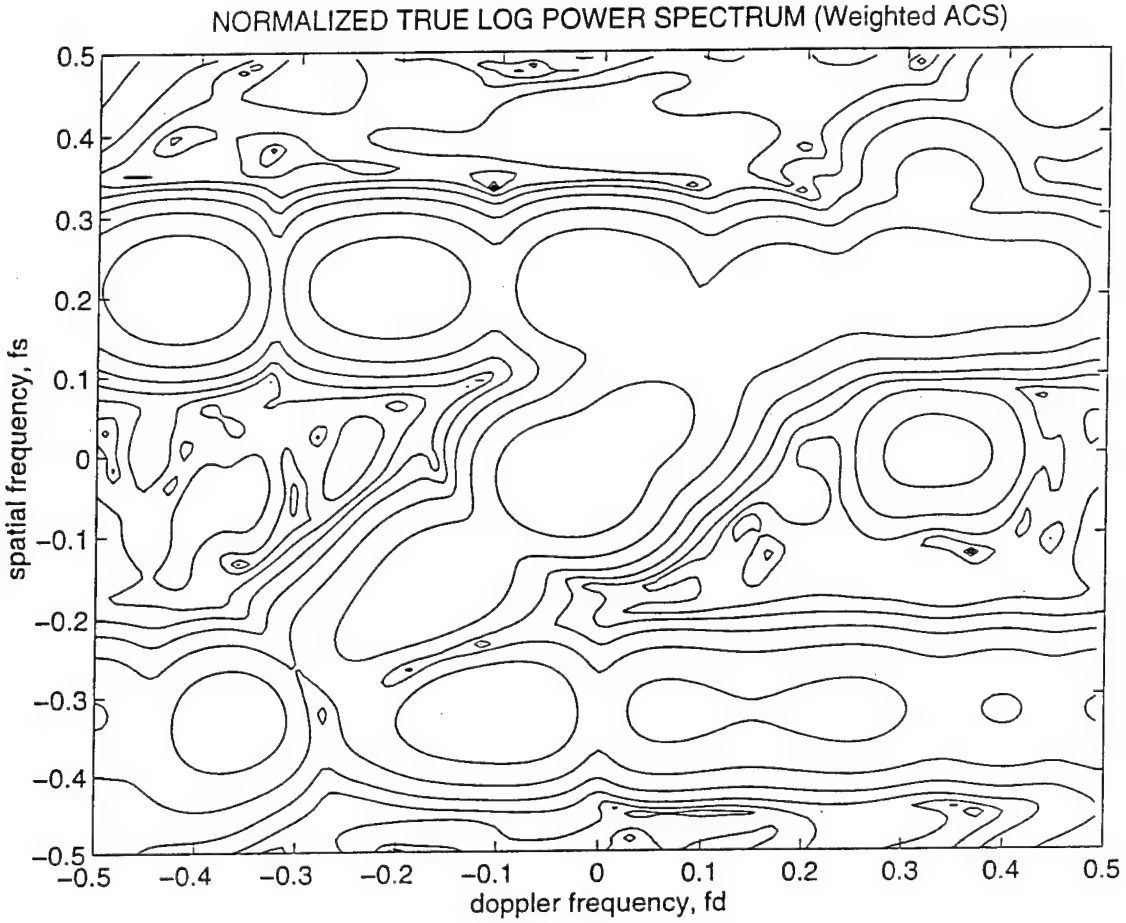


*Figure 3-4. Contour plot of the logarithm of the normalized true power spectrum of the array output for Ward's baseline case (DFT of the Dolph-Chebyshev weighted ACS).*

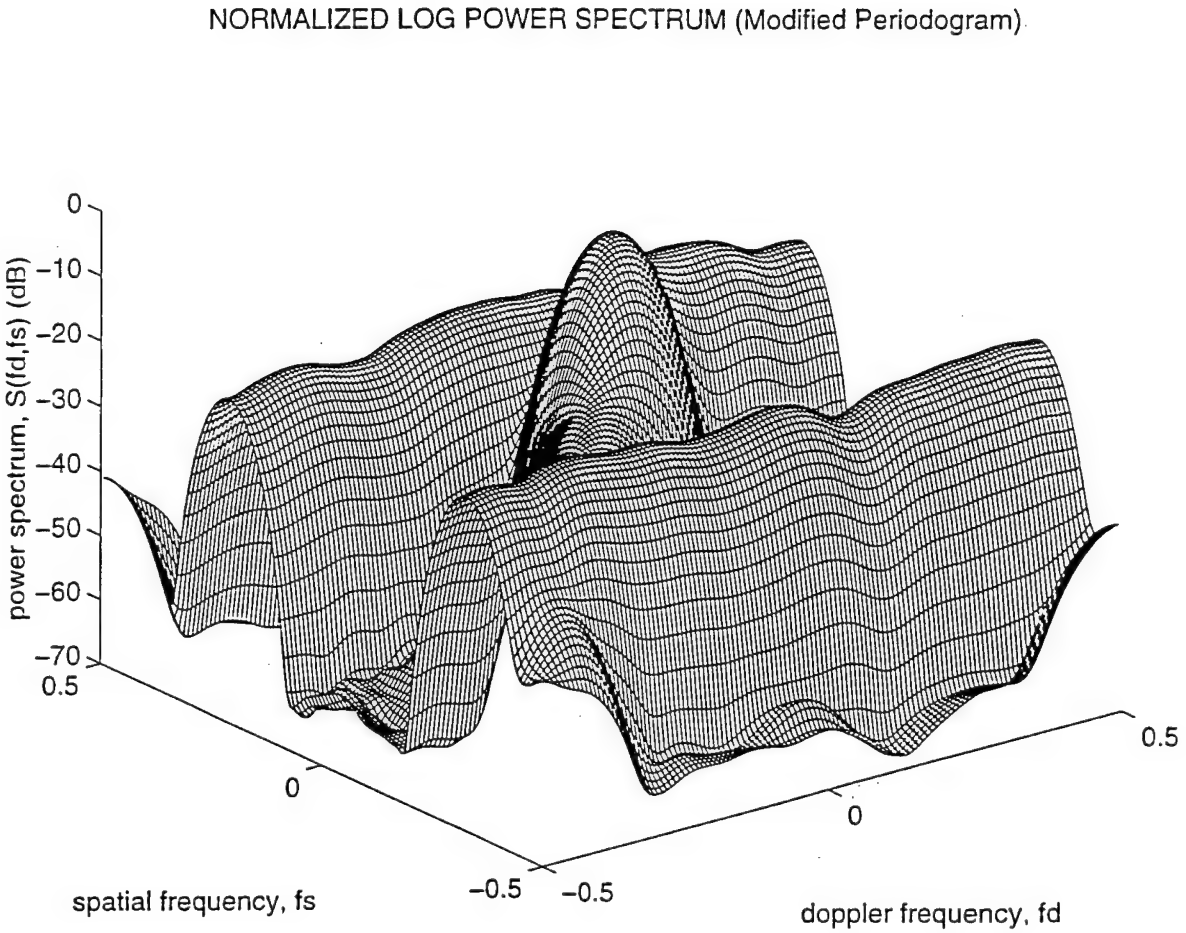


*Figure 3-5. Logarithm of the normalized power spectrum of the array output for Ward's baseline case (average of ten periodograms with Dolph-Chebyshev data weighting).*

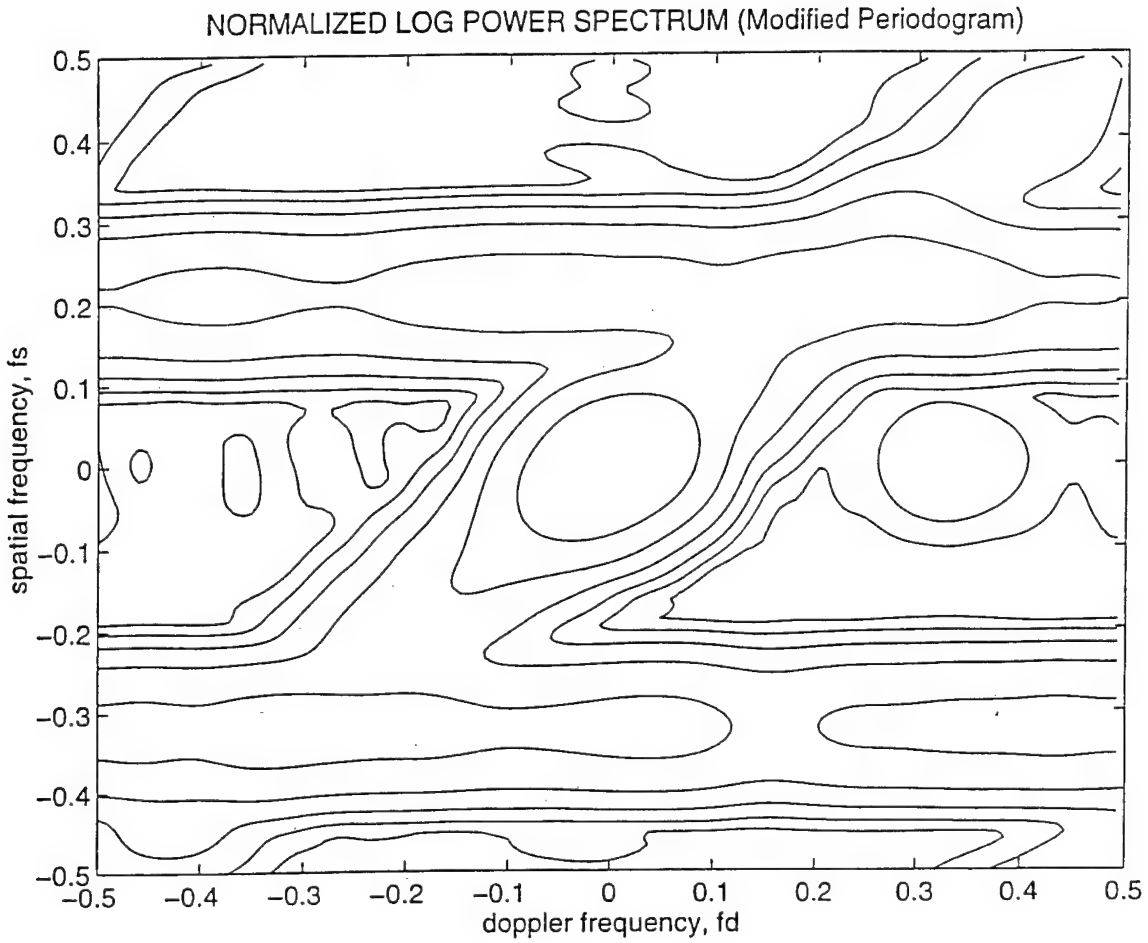


*Figure 3-6. Contour plot of the logarithm of the normalized power spectrum of the array output for Ward's baseline case (average of ten periodograms with Dolph-Chebyshev data weighting).*

## 4.0 CONCLUSIONS AND RECOMMENDATIONS

An analytic model for the multichannel signal in an airborne surveillance phased array radar for moving target detection is presented herein. The model includes target, ground clutter, broadband interference (jamming), and receiver noise components. The ground clutter component is the most complex, and is derived from the analytic model proposed by Jaffer et al. (1991), and adopted recently by Ward (1994). Several diagnostic issues are discussed also, including the transformation of a one-dimensional vector sequence into a two-dimensional scalar sequence, and the estimation of power spectra for space-time processes. A MATLAB-based software program was developed based on the analytic model, and has been tested thoroughly. The software model provides the means to generate representative multichannel radar data in an efficient and controlled manner.

The model discussed herein has been utilized to generate state space models for the ground clutter component in space-time processes, and to evaluate the multichannel innovations-based detection algorithm formulated in Phase I of the "Multichannel System Identification and Detection Using Output Data Techniques" SBIR program. These results are presented in the companion Volume I of this Final Technical Report (Román and Davis, 1996).

Various enhancements to the model have been identified for development in future programs. These include adding the capabilities to model: (a) internal clutter motion; (b) antennae element coupling; (c) return from multiple range rings; (d) different types of jammers; and (e) terrain-scattered interference ("hot clutter").

## REFERENCES


D. E. Dudgeon and R. M. Mersereau
(1984) Multidimensional Digital Signal Processing, Prentice-Hall, Inc., Englewood Cliffs, NJ.

J. E. Hudson
(1981) Adaptive Array Principles, Peter Peregrinus Ltd., New York, NY.

A. G. Jaffer, M. H. Baker, W. P. Ballance, and J. R. Staub
(1991) Adaptive Space-Time Processing Techniques for Airborne Radars, RL Technical Report No. RL-TR-91-162, Rome Laboratory, Rome, NY.

R. A. Monzingo and T. W. Miller
(1980) Introduction to Adaptive Arrays, J. Wiley & Sons, Inc., New York, NY.

F. E. Nathanson
(1991) Radar Design Principles (Second Edition), McGraw-Hill, Inc., New York, NY.

A. V. Oppenheim and R. W. Schafer
(1975) Digital Signal Processing, Prentice-Hall, Inc., Englewood Cliffs, NJ.

J. R. Román and D. W. Davis
(1996) Multichannel System Identification and Detection Using Output Data Techniques - Phase II, Vol. I, RL Technical Report, Rome Laboratory, Rome, NY.

M. I. Skolnik (editor-in-chief)
(1970) Radar Handbook, McGraw-Hill Book Co., New York, NY.

M. I. Skolnik
(1980) Introduction to Radar Systems (Second Edition), McGraw-Hill Book Co., New York, NY.

H. Urkowitz, J. D. Geisler, and N. A. Ricciardi, Jr.
(1973) "The effect of weighting upon signal-to-noise ratio in pulse bursts," IEEE Transactions on Aerospace and Electronic Systems, Vol. AES-9, No. 4 (July), pp. 486-494.

J. Ward
(1994) Space-Time Adaptive Processing for Airborne Radar, Technical Report No. TR-1015 (December), contract no. F19628-95-C-0002, Lincoln Laboratory, Massachusetts Institute of Technology, Lexington, MA.

*U.S. GOVERNMENT PRINTING OFFICE: 1997-509-127-47192

# *MISSION OF ROME LABORATORY*

Mission. The mission of Rome Laboratory is to advance the science and technologies of command, control, communications and intelligence and to transition them into systems to meet customer needs. To achieve this, Rome Lab:

a. Conducts vigorous research, development and test programs in all applicable technologies;

b. Transitions technology to current and future systems to improve operational capability, readiness, and supportability;

c. Provides a full range of technical support to Air Force Material Command product centers and other Air Force organizations;

d. Promotes transfer of technology to the private sector;

e. Maintains leading edge technological expertise in the areas of surveillance, communications, command and control, intelligence, reliability science, electro-magnetic technology, photonics, signal processing, and computational science.

The thrust areas of technical competence include: Surveillance, Communications, Command and Control, Intelligence, Signal Processing, Computer Science and Technology, Electromagnetic Technology, Photonics and Reliability Sciences.